EXPERIMENTAL INVESTIGATION OF THE EFFECT OF PHASE
TRANSFORMATION ON FRACTURE PARAMETERS OF NiTi SHAPE
MEMORY ALLOY

by

Behrouz Haghgouyan

B.S., Mechanical Engineering, Islamic Azad University-Tabriz Branch, 2008

Submitted to the Institute for Graduate Studies in

Science and Engineering in partial fulfillment of

the requirements for the degree of

Master of Science

Graduate Program in Mechanical Engineering

Boğaziçi University

2013

EXPERIMENTAL INVESTIGATION OF THE EFFECT OF PHASE
TRANSFORMATION ON FRACTURE PARAMETERS OF NiTi SHAPE
MEMORY ALLOY

APPROVED BY:

Prof. Günay Anlaş ....
(Thesis Supervisor)

Assist. Prof. C. Can Aydıner ....

Assist. Prof. Kadri Can Atlı ....

DATE OF APPROVAL: 06.08.2013

ACKNOWLEDGEMENTS

ABSTRACT

EXPERIMENTAL INVESTIGATION OF THE EFFECT OF PHASE TRANSFORMATION ON FRACTURE PARAMETERS OF NiTi SHAPE MEMORY ALLOY

This thesis aims to investigate the effect of martensitic phase transformation on fracture parameters of Nickel-Titanium (NiTi) SMA. NiTi specimens were characterized using optical microscopy and uniaxial tensile testing. 1mm thick compact tension (CT) coupons were cut to determine critical stress intensity factor (K_C) and crack tip opening displacement (CTOD) under Mode-I loading at room temperature. To observe the effect of martensitic phase transformation, tests were also carried out above martensite desist temperature (M_d) at which the stress induced phase transformation is suppressed. The results revealed that the martensitic phase transformation ahead of the crack tip, improves the fracture behavior of NiTi SMA. Finite elements, ABAQUS was also used to solve the 2-D cracked CT specimen problem under Mode-I loading. Shape and size of the transformation at the crack tip were examined, displacement and stress distribution near the crack tip were obtained. K_C and CTOD values were also calculated using J-integral for both superelastic and austenitic NiTi. FE analysis also revealed that the phase transformation enhances the toughness of Nitinol. The numerical results were compared to those obtained from tests and a good agreement was observed.

ÖZET

NiTi ŞEKİL HAFIZALI ALAŞIMINDA FAZ DÖNÜŞÜMÜNÜN KIRILMA PARAMETRELERİ ÜZERİNE ETKİSİNİN DENEYSEL OLARAK İNCELENMESİ

Bu tezde, martensitik faz dönüşümünün NiTi şekil hafızalı alaşımının kırılma parametreleri üzerine etkisi çalışılmıştır. Malzeme, optik mikroskop ve çekme deneyleri ile karakterize edilmiştir. K_C ve CTOD gibi kırılma tokluğu parametreleri, 1mm kalınlıktaki CT numuneler kullanarak oda sıcaklığında hesaplanmıştır. Martensit faz dönüşümünün kırılma parameterleri üzerine etkisini görebilmek amacıyla, deneyler faz dönüşümünün engellendiği sıcaklıkta M_d üzerinde tekrarlandı. Sonuçlar martensit faz dönüşümünün, NiTi ŞHA'nın kırılma tokluğunu artırdığını göstermiştir. Deneysel çalışmaların yanı sıra, sonlu elemanlar yöntemi ve ABAQUS programını kullanarak, 2-D çatlaklı modeller analiz edildi. Çatlak ucunda oluşulan transformasyon bölgesi ölçüldü ve gerilim dagılımı incelendi. J-integral parametresi kullanılarak, K_C ve CTOD değerleri süperelastik ve ostenitik NiTi ŞHA için elde edildi. Deneysel sonuçlar gibi, nümerik sonuçlar da martensit faz dönüsümünün, NiTi ŞHA'nın kırılma tokluğunu artırdığını göstermiştir. Ayrıca, deneysel ve sayısal sonuçlar karşılaştırıldığında, sonuçlar arasında uyum sağlandığı tespit edilmiştir.

TABLE OF CONTENTS

LIST OF FIGURES

LIST OF TABLES

LIST OF SYMBOLS

a	Crack Length
A_f	Austenite Finish Temperature
A_f^σ	Austenite Finish Temperature under Applied Stress
A_p	Area under the Load versus v_p
A_s	Austenite Start Temperature
A_s^σ	Austenite Start Temperature under Applied Stress
B	Specimen Thickness
E	Elastic Modulus
E'	Effective Elastic Modulus
f	Geometry Function
K	Stress Intensity Factor
K_I	Mode-I Stress Intensity Factor
$\dot{K}$	Rate of Increase of Stress Intensity Factor
K_C	Fracture Toughness
K_{IC}	Plain Strain Fracture Toughness
m	Function of σ_{YS}/σ_{UTS}
M_d	Martensite Desist Temperature
M_f	Martensite Finish Temperature
M_f^σ	Martensite Finish Temperature under Applied Stress
M_s	Martensite Start Temperature
M_s^σ	Martensite Start Temperature under Applied Stress
N_A	Number of Annealing
P	Applied Load
P_{max}	Maximum Applied Load
r	Radial Polar Coordinate
r_y	Radius of the Plastic Zone
T_0	Reference Temperature
u_y	Displacement Component in y Direction

v_p	Plastic Component of Clip Gauge Opening Displacement
W	Specimen Width
x	Cartesian Coordinate Axis
y	Cartesian Coordinate Axis
z	Cartesian Coordinate Axis
$\dot{\Delta}_{LL}$	Testing Machine Loading Rate
ϵ^L	Transformation strain
ϵ^L_V	Volumetric Transformation strain
η	Geometry Function
θ	Angular Polar Coordinate
κ	Function of ν
ν	Poisson's Ratio
ν_A	Austenite Poisson's Ratio
ν_M	Martensite Poisson's Ratio
σ	Remote Stress
σ^{Af}	Austenite Finish Stress
σ^{As}	Austenite Start Stress
σ^A_Y	Austenite Yield Stress
σ^{Mf}	Martensite Finish Stress
σ^{Ms}	Martensite Start Stress
σ^M_Y	Martensite Yield Stress
σ_f	Finishing Stress of Detwinning
σ_s	Starting Stress of Detwinning
σ^S_L	Start of Transformation Stress in Loading
σ^E_L	End of Transformation Stress in Loading
σ^S_U	Start of Transformation Stress in Unloading
σ^E_U	End of Transformation Stress in Unloading
σ^S_{CL}	Start of Transformation Stress in Compression
$\left(\frac{\delta\sigma}{\delta T}\right)_L$	Slope of $\sigma - T$ Diagram during Loading
$\left(\frac{\delta\sigma}{\delta T}\right)_U$	Slope of $\sigma - T$ Diagram during Unloading

σ_{YS}	Yield Stress
σ_{UTS}	Ultimate Tensile Stress
σ_{xx}	Normal Stress Component in x Direction
σ_{yy}	Normal Stress Component in y Direction
σ_{zz}	Normal Stress Component in z Direction
τ_{xy}	Shear Stress in xy Plane
τ_{xz}	Shear Stress in xz Plane
τ_{yz}	Shear Stress in yz Plane

LIST OF ACRONYMS/ABBREVIATIONS

2-D	Two Dimensional
CMOD	Crack Mouth Opening Displacement
COD	Crack Opening Displacement
CT	Compact Tension
CTOD	Crack Tip Opening Displacement
DIC	Digital Image Correlation
DSC	Differential Scanning Calorimetry
EDM	Electro Discharge Machining
EPFM	Elastic Plastic Fracture Mechanics
LEFM	Linear Elastic Fracture Mechanics
LLD	Load Line Displacemenet
LPS	Lower Plateau Stress
NiTi	Nickel-Titanium
Nitinol	Nickel-Titanium Naval Ordnance Laboratory
RD	Rolling Direction
SEM	Scanning Electron Microscopy
SMA	Shape Memory Alloy
TD	Transverse Direction
UPS	Upper Plateau Stress

1. INTRODUCTION

1.1. Shape Memory Alloys

Because of their interesting properties, Shape memory alloys (SMAs) drew scientists' attention and became a major topic of research in many fields. These alloys are capable of recovering from large strains upon heating (shape memory effect) or through removal of load (superelasticity or pseudoelasticity) that are associated with martensitic transformation. Superelasticity and shape memory effect have been observed in many alloys such as Au-Cd, Ni-Ti, Ni-Mn-Ga, Cu-Al-Ni, Cu-Zn-Al, etc. Among these, Ni-Ti is the most popular shape memory alloy because of its features such as biocompatibility, wear resistance, corrosion resistance and high recoverable strain.

NiTi, a nearly equiatomic mixture of Nickel and Titanium, is the most known and used shape memory alloy. In 1962 William J. Buehler was working on a project for U.S. Navy when he discovered that Nickel-Titanium alloy returns to its original shape as a with change in temperature. This alloy was later named Nitinol, an acronym for Nickel-Titanium Naval Ordnance Laboratory. In NiTi, parent phase is cubic and the product phase is monoclinic. NiTi is capable of recovering strains up to approximately 8% [1].

1.2. Martensitic Phase Transformation

Martensitic phase transformation is a solid to solid diffusionless transformation between two phases that can be induced either by a change in temperature or stress. The parent phase, called austenite, which has generally a cubic crystal structure, has high-symmetry and is stable at high temperature. The product phase, called martensite, is the low-temperature, low-symmetry phase with a tetragonal, orthorhombic or monoclinic crystal structure.

Each martensitic crystal formed can have a different orientation, called a variant. The assembly of martensitic variants can exist in two forms: twinned martensite, which is formed by a combination of self-accommodated martensitic variants, and detwinned or reoriented martensite in which a specific variant is dominant [1]. The self-accommodated martensite forms when the transformation is induced by temperature. The detwinned martensite, on the other hand, forms when the martensitic phase is induced by stress.

The martensitic transformation is reversible. The transformation from austenite to martensite is named forward transformation and the transformation from martensite to austenite is called reverse transformation. There are four characteristic temperatures at which the martensitic phase transformation occurs:

- M_s: Martensite Start Temperature,
- M_f: Martensite Finish Temperature,
- A_s: Austenite Start Temperature,
- A_f: Austenite Finish Temperature.

Upon cooling, the forward transformation begins at the martensitic start temperature (M_s) and finishes at the martensitic finish temperature (M_f). Similarly, during heating, the reverse transformation initiates at the austenitic start temperature (A_s) and finishes at the austenitic finish temperature (A_f).

Stress and temperature have a significant effect on the martensitic transformation. As shown schematically in Figure 1.1, transformation start and finish stresses strongly depend on temperature in a way that transformation stresses increase with an increase in temperature. Consequently, the new transformation stresses are represented as σ^{Ms}, σ^{Mf}, σ^{As} and σ^{Af}. In this figure, the σ_s and σ_f are the starting and finishing stresses of detwinning, respectively. It is worth mentioning that when the applied stress is greater than σ_s (the stress at which the forward transformation starts), the forward phase transformation will result in the direct formation of detwinned martensite. Note that the transformation desist temperature (M_d), is the intersection of M_s line and σ_Y^A.

The latter denotes the critical stress for slip of austenite. In a similar way, the stress affects the transformation start and finish stresses. As shown schematically in Figure 1.1, transformation start and finish stresses increase with an increase in temperature.
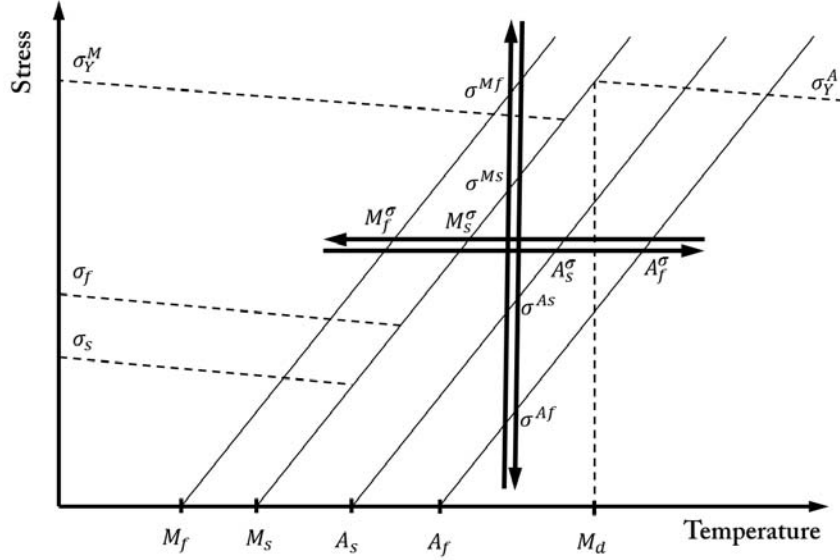
Figure 1.1. Schematic of transformation temperatures variation in the presence of applied load.

1.3. Shape Memory Effect

The nature of the shape memory effect can be explained on a stress-temperature-strain space. Figure 1.2 shows the stress-temperature-strain curve of a typical NiTi. According to this figure, at point A, the material is in austenite phase. Decreasing the temperature, results in forward transformation. At temperature below M_f the material is twinned martensite (Point B). Afterwards, stress is applied and the twinned martensite is reoriented into detwinned martensite, up to the point C. Upon removal of the load, the elastic strain is recovered, but some permanent deformation remains (Point D). At this point, increasing the temperature initiates the reverse transformation. When the temperature reaches A_f, the SMA fully transforms to austenite and returns to its original shape (point A). Cooling from point A to B, results in the formation of self-accommodated variants, with no associated shape change [1].
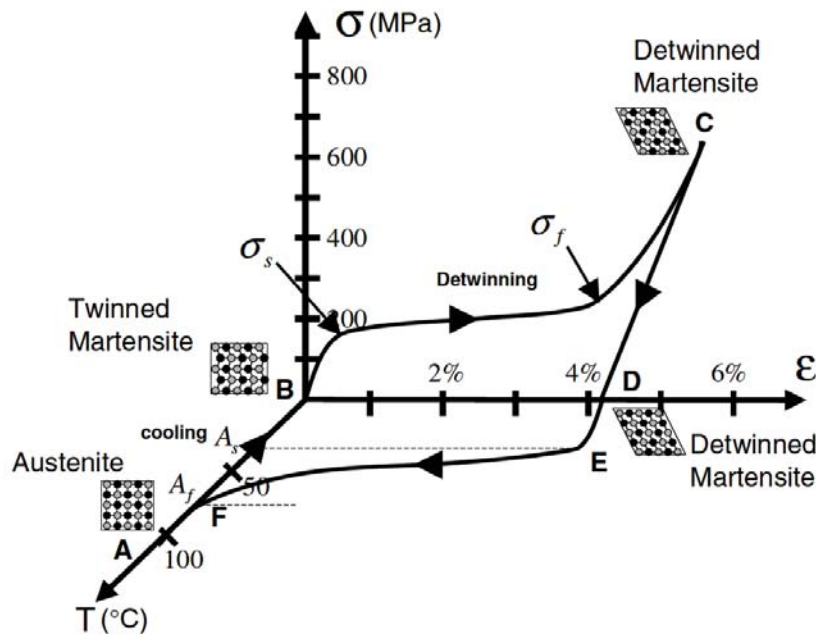
Figure 1.2. Stress-strain-temperature data exhibiting the shape memory effect for a typical NiTi [1].

1.4. Superelasticity

SMAs can recover from large amount of strains (approximately 8% for a typical NiTi). A schematic representation of superelastic stress-strain diagram is shown in Figure 1.4. At point A, the material is above austenite finish temperature A_f , but below martensite desist temperature M_d. The latter denotes the temperature at which the stress to induce martensite is equal to the stress to plastically deform austenite. In other words, M_d is the temperature upon which the stress induced phase transformation is suppressed. At point A, the SMA is in austenite state because the temperature is above the austenite finish temperature A_f. When stress is applied to the material, it responds elastically until point B. At this point, the stress reaches a critical value (σ^{Ms}) whereupon a transformation from austenite to detwinned martensite occurs. During transformation, the stress remains almost constant and a stress plateau is formed until point C. At this point with a stress value of σ^{Mf}, material is fully transformed to detwinned martensite. Upon further loading, the detwinned martensite behaves in

an elastic manner. Further loading results in plasticity of detwinned martensite and eventually failure. Upon unloading within elastic region of martensite (Point D), a reverse transformation takes place due to the fact that martensite is energetically less favorable compared to austenite without stress at temperatures above A_f. The reverse transformation from martensite to austenite occurs at a lower stress than σ^{Ms} resulting in a hysteresis effect in stress-strain curve. When stress reaches the value σ^{As} (Point E), the reverse phase transformation starts and the detwinned martensite transforms back to austenite. The reverse transformation is completed when the stress reaches σ^{Af}. From point F, the austenite is unloaded elastically to the point A and the initial shape with no permanent deformation is recovered.
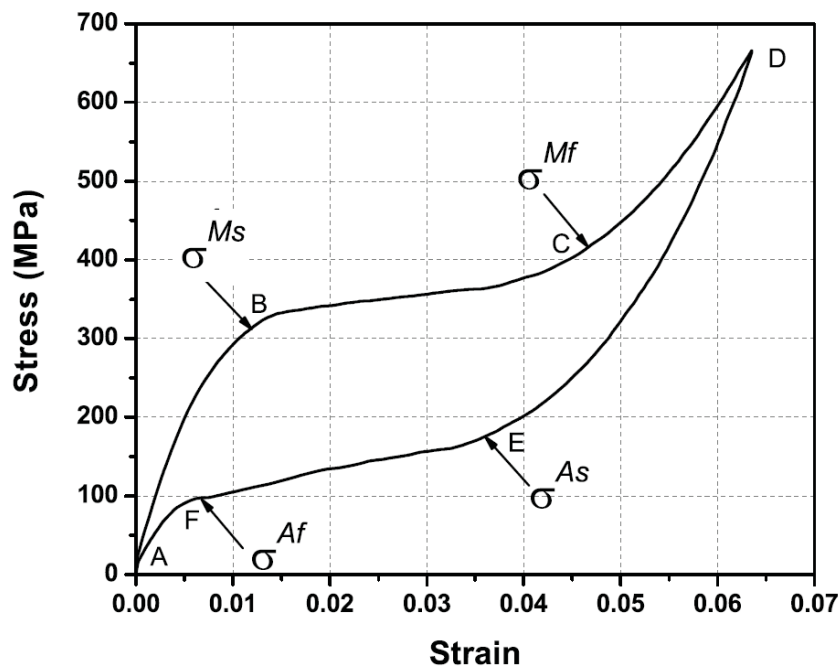
Figure 1.3. Superelastic stress-strain curve of a typical SMA [1].

1.5. Applications

In aerospace industry, SMAs are generally used as actuators. Using SMAs for such purposes, simplifies the design compared to electro-mechanical actuation mechanism. Moreover, it reduces the weight of the mechanism by eliminating extra parts. For

instance, the shape memory effect has been used in latches on the solar panels of the Hubble Space Telescope. These latches kept the solar panels down until it was safe to deploy them, at which point the latches were heated and returned to their original (unlatched) shape, releasing the panels [2]. SMAs are used in Mars Pathfinder as part of an actuation mechanism for an instrument that measure dust collection on the surface of Mars [3] .

SMAs can be used as couplings and fasteners because of their shape memory property. The procedure is quite simple. The SMA coupling is processed in ambient temperature. Then the diameter is enlarged in low temperatures. After installing on desired location which should be joined or fastened, the device is then heated up to ambient temperature. Consequently it recovers the initial shape and fastens parts. Raychem Corporation in 1969, used SMAs in cryogenic aircraft pipe fitting devices for fuel systems. More than one hundred thousand of these fittings have been installed in advanced airplanes such as the F-14 and there have been no reported failures [3].

The shape memory effect was used in the middle 70's to design the prototype heat engine. The concept that SMAs can produce large forces when subjected to temperature differences was used by Banks to design this heat engine. However, it has only been used for demonstration purposes [4].

In addition to shape memory effect and superelasticity, biocompatibility and corrosion resistance make SMAs, in particular NiTi, a good solution for variety of biomedical applications such as stents, guide wires, orthodontic devices, artificial joints, etc. Superelasticity is useful in a wide variety of medical applications, most notably in the stent design. Stent is a mesh tube inserted into a vessel in the body to prevent contraction and improve the blood flow. It could be used either permanently to reinforce blood vessels or temporarily to hold a vessel open to allow access for surgery. Stents are manufactured with a diameter larger than that of target vessel. It is then compressed and inserted with a wire in the desired place inside the vessel. After releasing, it expands due to the superelasticity and increases the diameter of the vessel. An example of biomedical application of shape memory effect is the Simon filter. It is used

as a filter that traps clots in blood vessels. It is deformed in low temperature, and constrained within a catheter. When the device is inserted into the desired location, the human body temperature expands it to the initial shape. SMA is also used to design orthodontic braces. The braces which are made from stainless steel get loose over time and they need to be adjusted periodically. SMA orthodontic braces however, provide nearly constant force over a long period of time.
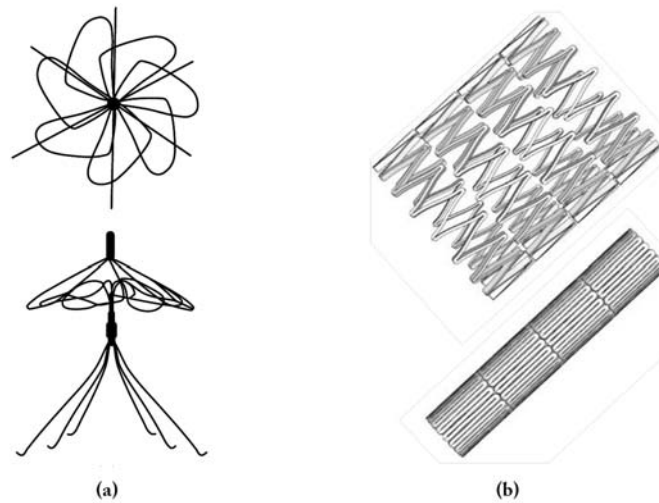
Figure 1.4. Cardiovascular devices that utilize the engineering properties of SMAs: (a) Top view (above) and side view (below) of the Simon filter in the deployed configuration, (b) a self-expanding NiTi stent shown in the deployed configuration (above) and constrained state (below) [1].

As mentioned earlier, the hysteresis effect is observed in stress-strain curve of SMAs demonstrating energy dissipation which can be quantified by the area inside of this hysteresis loop. This characterization has been employed for energy absorption in damping systems in both mechanical devices and seismic structures [5].

SMAs are used in some commercial applications such as eyeglass frames, cellular telephone antennas, and golf clubs because of their superelastic properties. SMA fibers could also be embedded into composites. The shape memory effect is employed in SMA rivets, clamps, seals etc.

1.6. Fracture in SMAs

High stress values cause crack tip yielding in metals. In a similar way, SMAs accommodate high stress through stress induced phase transformation. In other words, when a superelastic SMA is subjected to loading, high values of stress induce martensitic transformation in the vicinity of crack tip. This stress induced martensite, plays a significant role on fracture of SMAs, as it changes the crack tip stress distribution unlike ordinary metals. As illustrated in Figure 1.5, three different regions can be observed in the vicinity of the crack tip of SMAs:

(i) The austenitic untransformed region (A),

(ii) The phase transformation region $(A \rightarrow M)$,

(iii) The fully transformed martensitic region (M).
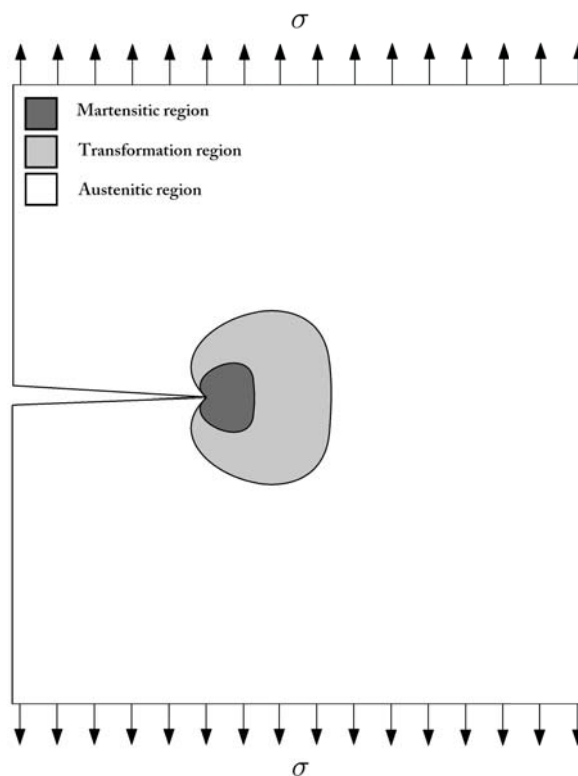
Figure 1.5. Schematic of the phase transformation region near the crack tip.

1.7. Literature Review

Early works on SMAs have been devoted to study of crystallography and thermo-dynamics of phase transformation. Later, constitutive laws were developed to describe stress-strain relations during transformation. As the use of the SMAs in variety of applications increased, the necessity to study and characterize their active properties, their failure behavior arose and started to dominate the recent studies on SMAs.

In 1995, Stam and van der Giessen [6], investigated the effect of phase transformation on shape and size of the transformation zone around crack tip in SMAs. They analyzed crack growth resistance under quasi-static condition analytically and numerically. They stated that the phase transformation increases the toughness of the material.

Birman in 1998 [7], analyzed Mode-I fracture of an SMA plate with a central crack. He adopted the constitutive theory of Tanaka to evaluate the size of the plastic zone in front of the crack. The influence of the phase transformation on the stress intensity factor was also studied. According to their results, the effect of the phase transformation on stress intensity factor is relatively small. As a result, they stated that properties of austenite state may be used to evaluate stress intensity factor.

In 2000, Yi and Gao [8], analytically investigated the fracture toughening mechanism of SMAs due to martensite phase transformation using Eshelby inclusion and weight function method. Analyzing asymptotic stress in semi-infinite cracks subjected to Mode-I loading, they found that martensite transformation reduces crack tip stress intensity factor and increases toughness. The shape and size of the transformation zone were also determined for static and steadily advancing crack.

Yi *et al.* proceeded to investigate the mixed mode loading case in 2001 [9]. They used the energy release rate and load phase angle instead of stress intensity factor to show that martensitic transformation reduces crack tip energy release rate and increases the toughness.

Yan *et al.* in 2003 [10], investigated the effect of plasticity on martensitic transformation of superelastic NiTi using a constitutive model that accounts for both phase transformation and plasticity. They described the forward and reverse transformation process by change of the martensite volume fraction. They discussed the influence of hydrostatic stress on transformation is discussed.

In 2008, Lexcellent and Thiebaud [11], carried out an analytical study to determine the transformation zone at the crack tip of SMAs showing asymmetry between tension and compression. They also compared results to those obtained from previous experimental studies on NiTi.

In 2010, Maletta and Furgiuele [12], developed a solution for plane stress under Mode-I loadings of NiTi based SMAs based on Irwin's correction of LEFM. They studied the extent of martensitic transformation around crack tip and the stress distribution in both transformed and untransformed regions. The results were compared to those from finite element simulations and a good agreement was observed. They also investigated the effect of various parameters such as transformation stress, transformation strain, Young's moduli, applied stress and temperature on crack tip transformation behavior. They stated that temperature plays a significant role on the extent of the transformation region, crack tip stress distribution and consequently fracture of NiTi.

In 2011, Lexcellent *et al.* [13], predicted the transformation zone at the crack tip of SMAs for loading modes 1, 2, 3 and mixed 1+2 using LEFM. They also did some tests to investigate the temperature field evolution during fracture of edge cracked NiTi specimens under Mode-I loading. They observed an increase in temperature in the vicinity of the crack tip.

Maletta and Furgiuele in 2011 [14], proposed new fracture control parameters for NiTi based SMAs by defining two stress intensity factors to describe stress distribution in austenitic region and transformed martensitic region near crack tip. According to their results, the stress intensity factor in austenite region is always greater than LEFM predictions, while the stress intensity factor in martensite region is always smaller. Con-

sequently, because fracture occurs in transformed martensitic region, transformation has a toughening effect. It was also revealed that temperature has a marked effect on both stress intensity factors.

Maletta and Young in 2011 [15], analytically predicted boundaries of the transformation zone and stress distribution at the crack tip of NiTi based SMAs using modified LEFM concepts. They compared their results to those obtained from synchrotron X-ray micro-diffraction mapping on CT specimens and a good agreement was observed. They also discussed the effect applied load and crack length on transformation zone.

In 2012, Maletta [16], predicted the extent of transformation region and stress distribution at crack tip of NiTi based SMAs by using an analytical model. Their model was based on small scale yielding assumption and EPFM theory, and was able to analyze SMAs with no constant transformation stress. They also studied the effect of non-constant transformation stress and its slope on transformation region and stress distribution at crack tip. They found a marked effect on transformation region and a small effect on stress intensity factor.

Baxevanis and Lagoudas in 2012 [17], studied Mode-I fracture of a center-cracked, infinite, pseudoelastic SMA plate under plane stress using Dugdale-Barenblatt model. They presented a closed form expression for J -integral, COD and transformation zone size. For the case of high remote stresses, a closed form expression for the J -integral was derived and transformation and plastic zone sizes were numerically evaluated.

Yan *et al.* numerically studied effect of volume contraction induced by phase transformation, on fracture properties of superelastic SMA in 2002 [18]. They analyzed the behavior of quasi-static advancing crack. According to the results, the volume contraction induced by phase transformation, increases the crack tip stress intensity factor and reduces the toughness of SMAs.

In 2005, Wang *et al.* [19], investigated martensitic transformation near crack tip of pseudoelastic NiTi SMAs. They implemented Aurichio's model into finite element code.

It was revealed that the amount of martensite and the extension of the transformed region in a sharp crack is larger compared to a mild notch and gets larger as crack grows.

Wang in 2006 [20], carried out finite element calculations in NiTi CT specimens with crack, with acute and blunt notches. He studied distribution of stress-strain and martensite volume fraction in front of crack/notch tips and analyzed their effects on fracture. He showed that with increasing the notch acuity from blunt notch through acute notch to crack, stress, strain and the full martensite zone size at the crack/notch tips increase, and crack growth changes from unstable to stable.

In another study by Wang in 2007 [21], stress and strain distribution in front of a notch tip in CT NiTi specimen was studied using finite elements. He considered two types of materials: first with a stress-induced martensite transformation and the other one a fully martensite. Comparing the mechanical behavior of these two materials, he analyzed the effect of martensite transformation on fracture behavior of NiTi. Wang observed that martensite phase transformation improves toughness.

In 2007, Freed and Banks-Sills [22], numerically studied transformation toughening behavior of cracks in SMAs under plain strain and Mode-I deformation. They used a cohesive zone model and obtained resistance curves. According to their results, the reversibility of transformation reduces the toughness of the alloy. The shape of the transformation zone and the effect of moduli mismatch between austenite and martensite on transformation toughening were also discussed.

In 2007, Wang [23], numerically investigated stress-strain and phase transformation in front of a notch tip in a NiTi CT specimen and found that the maximum strain always appears at the notch tip and then decreases with the distance away from the notch tip. Four different regions were observed at different loading stages for the stress distribution in front of the notch tip due to martensitic transformation and subsequent plastic deformation. He predicted that the fracture initiation takes place in plastic zone at the crack tip and martensitic transformation at the crack tip improves the

toughness of SMAs.

Falvo *et al.* in 2009 [24], studied martensitic transformation in front of a crack tip of single edge-crack specimens in NiTi SMA using 2-D finite element simulations. The effect of temperature on stress-strain distribution and transformation boundaries were also analyzed using Clausius-Clapeyron relation. According to numerical results, the transformation zone reduced with increasing temperature. Comparing the results obtained by finite elements to analytical results obtained by Irwin's modified LEFM relations, a good agreement was observed in terms of transformation boundaries.

Baxevanis *et al.* in 2012 [25], studied shape and size of transformation and plastic zones near the crack tip of a pseudoelastic SMA. A small scale transformation assumption under plane strain was used. The J-integral fracture toughness was studied. The results were compared to those of elastic-plastic materials. Baxevanis *et al.* observed that increasing temperature results in decreasing transformation zone size, while the dependence of the plastic zone size on temperature is less. They also observed that the J-integral is path dependent. According to the results, the difference between the crack tip and far-field J-values in SMAs is smaller than the corresponding difference in elastic-plastic materials.

In 2013, Baxevanis *et al.* [26], studied the quasi-static stable crack growth in shape memory alloys under plane strain and Mode-I using finite elements calculations. They employed small scale transformation assumption and studied transformation toughening behavior. Results showed an enhancement as a result of stress-induced phase transformation. The effect of plastic dissipation on fracture resistance of SMAs was also studied revealing that plastic dissipation during crack growth is only a small fraction of energy dissipated as a result of phase transformation.

Gall *et al.* studied fracture of single crystal and polycrystalline NiTi SMA using SEM in 2001 [27]. Nucleation, growth, and coalescence of voids from the Ti_3Ni_4 precipitates or Ti-C inclusions besides cleavage fracture, were observed during fracture of NiTi. They found that as the Ti_3Ni_4 precipitate size increased, a transition to more

ductile local fracture mechanisms was observed. They also observed that polycrystalline samples showed a more ductile fracture surface appearance compared to the case of single crystal.

Tong *et al.* in 2003 [28], investigated crack initiation and growth in NiTi carrying out tension tests on single-edge notched sheets. They used DIC to obtain in-plane deformation field at the crack tip. CTOD and CTOA were also calculated using crack tip deformation data. SEM showed that fracture surface of NiTi sheet was dimpled. They observed large scale yielding over large region ahead of crack tip in thin sheets. Their observations revealed that nucleation, growth, and coalescence of voids from the Ti_3Ni_4 precipitates were responsible for the crack initiation and growth.

In 2005, Chen *et al.* [29], investigated the fracture behavior of NiTi at room temperature using tension, three point bending and four point bending specimens. They performed macroscopic mechanical tests and microscopic in situ observations via SEM to study the crack initiation and growth. They observed that, the crack propagates with a quasi-cleavage mode along the direction of maximum normal stress. They concluded that martensitic transformation improves the toughness of NiTi.

In 2007, Daly *et al.* [2], experimentally investigated fracture properties of edge-cracked thin sheets of NiTi. They observed strain fields in the vicinity of crack tip by means of DIC. Using the strain field, they determined shape and size of the saturation and transformation zones. An average fracture toughness (K_C) was measured using LEFM and it was revealed that the phase transformation contributes to toughening.

Robertson *et al.* studied crack growth in superelastic NiTi in 2007 [30]. They measured in situ three-dimensional strains, phases and crystallographic alignment by means of synchrotron X-ray micro-diffraction. They found that crack propagation always occurs in the fully transformed martensite. They found that the stress-induced transformation provides a mechanism of renormalizing the stressed zone in a way that the resulting reduction in the stress field near a crack improves fracture resistance. They also observed that the transformation zone at the crack tip was peanut shaped,

consistent with LEFM anisotropic yield criteria. According to their results, the two-phase region is only stable in a narrow stress range.

Jiang and Vecchio in 2007 [31], investigated the fracture behavior of NiTi under quasi-static and dynamic loading conditions. They used pre-cracked bend samples to measure the dynamic fracture initiation toughness. According to the results, the dynamic fracture toughness of NiTi is higher than it is under quasi-static loading.

Wang *et al.* in 2008 [32], investigated the fracture behavior of pseudoelastic NiTi. Performing fracture experiments using CT specimens, they obtained K_{IC} of the material. SEM was used to observe fracture surfaces and it was that fracture mechanism is dominated by cleavage. According to results obtained using finite elements, there is always a small fully transformed region at the crack tip during fast fracture process.

In 2008, Gollerthan *et al.* [33], investigated behavior of a martensitic/pseudoplastic NiTi using CT specimens. They used the LEFM approach to measure critical stress intensity factors and obtain estimates on dimensions of pseudoplastic zones in front of crack tips. However, LEFM couldn't rationalize results because the mechanical behavior of martensitic NiTi CT specimens clearly involves large-scale reorientation and growth of favorably oriented martensite variants.

In 2008, Creuziger *et al.* [34], used notched Mode-I fracture samples to examine phase transformation in single crystal NiTi. Using optical techniques in situ and considering two different crystallographic orientations (the [100] and [111] directions), they found that in the [100] notched samples stable crack growth was observed; in the [111] notched samples however, crack propagated in an unstable manner. They also stated that transformation around the notch is important in crack growth behavior.

Wang *et al.* [35], studied the effect of notches on fracture behavior of NiTi in 2009. They carried out fracture experiments on specimens with different notch types and sizes. Finite element simulations were performed to analyze stress, plastic strain and phase transformation fields. It was revealed that both the transformation zone

and plastic zone are concentrated to the notch/crack tip with increasing notch acuity. Fracture surfaces were examined using SEM. They observed that cracks initiated in the mid-plane of the specimens, where the stress is maximum according to finite element analysis. It was also observed that void nucleation, growth and coalescence of micro cracks dominated the failure of specimens without notch and with semi-circular notches. However, in the specimen with crack notch, cleavage fracture dominated the fracture.

In 2009, Gollerthan et $al.$ [36], investigated crack extension under static loading of NiTi using CT specimens in three material states: martensitic and pseudoelastic austenitic at room temperature and austenite at temperature above M_d. They performed fracture tests and used linear elastic fracture mechanics approach. They observed that crack propagation in pseudoelastic and austenitic NiTi alloys is unstable. In contrast, martensitic alloy shows slow crack propagation. Crack tip blunting was not observed in the martensitic and pseudoelastic SMAs. According to this study, cracks grow into detwinned martensitic variant microstructures in martensitic and pseudoelastic NiTi and crack propagation occurred at similar stress intensities. In contrast, in austenitic NiTi tested above M_d, cracks grow into austenite without martensite at the crack tip and crack propagation starts at higher stress intensities.

Jiang et $al.$ in 2012 [37], performed tensile and compressive tests on round tensile samples to study fracture behavior of as cast NiTi. According to the results obtained from microanalysis of fractured samples, under tensile test at high temperature, the alloy showed high plasticity and the fracture was characterized by ductile fracture, while poor plasticity and cleavage fracture were observed at room temperature.

Maletta et $al.$ in 2013 [38], investigated fracture properties of pseudoelastic NiTi by analytical studies, finite element simulations and experimental measurements. They analyzed the phase transition mechanisms and resulting stress distribution at the crack tip of single edge cracked specimens in different temperatures. They compared the results obtained from analytical model with those obtained from finite element simulations and observed a good agreement. The experimental results were analyzed by LEFM and modified stress-intensity factors were calculated using the analytical

model which is based on Irwin's correction for elastic-plastic materials. The results revealed that the critical stress intensity factor slightly increases with increasing the testing temperature. The fracture surfaces were also analyzed using scanning electron microscopic. SEM results revealed a dimpled appearance typical of ductile fracture mechanisms, and no significant differences have been observed between the different testing temperatures.

1.8. Problem Statement and Objective

Although there have been recent developments in modeling and numerical analysis of fracture in SMAs, there is room for further experimental work. Most of the experimental works contain study of microstructure of fracture surface or observing crack initiation and growth in cracked or notched specimens with optical techniques such as optical microscopy, scanning electron microscopy (SEM), synchrotron X-ray microdiffraction, etc. There are relatively few studies on fracture toughness, which generally include fracture toughness measurement of bulk material. Very few experiments have investigated the thickness range of 1 mm. Since the fracture toughness depends on the thickness and according to the fact that NiTi are often used in most of the applications such as medical devices, in the form of thin sheets, direct experimental characterization of the fracture parameters of this thickness range is desirable. In addition to the previous points, understanding of the effect of phase transformation on the fracture properties of SMAs is as yet incomplete. Some studies [18, 36], demonstrated that the phase transformation decrease the toughness of the SMAs. On the other hand, according to other studies [2, 8, 14, 21, 26, 29], the martensitic phase transformation has a toughening effect. Consequently there is a need to further investigate the transformation effect on toughness of these alloys. This is crucial for the effective design and performance of SMA devices.

The objective of this study is to investigate the effect of martensitic transformation on fracture parameters of NiTi SMA. To this aim, fracture tests are carried out to measure fracture toughness both at room temperature and high temperature. Considering the fact that stress induced martensite transformation is suppressed above

a specific temperature (M_d), the effect of this transformation is studied comparing results obtained at two different temperatures. In addition, finite element was used to compare the numerical results to experimental. Interpretation of numerical and experimental measurements is intended to contribute to discussion on fracture of NiTi structures.

The structure of this thesis is as follows: In Chapter 2, the material is characterized using optical microscopy, differential scanning calorimetry (DSC) and uniaxial tensile tests. In the first section of Chapter 3, load-displacement curves are obtained for NiTi CT specimen and critical stress intensity factor is measured at both room temperature and high temperature. In subsequent section, crack tip opening displacement is measured at two different temperatures. In Chapter 4, finite element analysis of 2-D CT specimens is presented. Transformation boundaries are determined, displacement and stress distribution ahead of the crack tip are investigated. In addition, K_C and CTOD are calculated using J-integral for superelastic and austenitic NiTi. In the last chapter, findings of this study are summarized.

2. MATERIAL CHARACTERIZATION

NiTi SMA sheets with 1 mm thickness and 55.99 wt.% Ni, which had been produced according to the ASTM F2063-12 (Standard Specification for Wrought Nickel-Titanium Shape Memory Alloys for Medical Devices and Surgical Implants) [39], were purchased from Johnson Matthey. The mechanical properties and chemical composition are presented in Table 2.1 and 2.2 respectively.

Table 2.1. Mechanical and physical properties of NiTi used in this study.

Temper	Surface	σ_{UTS} (ksi)	Elongation (%)	A_f (°C)
Flat Annealed	Pickled	220	12.7	16.1

Table 2.2. Chemical composition of NiTi used in this study.

	Ni	Ti	C	O	Co,Cr,Cu,Fe,Mn,Mo,Nb,Si,W
Weight (%)	55.99	Bal.	< 0.05	< 0.05	< 0.2

It is worth noting that the data are taken from the data sheet of the material provided by the supplier. Since the mechanical properties presented were limited, additional tests were carried out to measure required parameters.

2.1. Microstructure

In order to estimate the grain size of the NiTi sheets, the microstructure was examined using optical microscopy. First, grinding was carried out manually using abrasive papers by decreasing the abrasive grit sequentially. Then the specimen was polished using polishing tabs with alumina abrasive. Finally, the specimen was etched in a solution containing HF, HNO$_3$ and H$_2$O with a volume ratio of 1:4:5 and then

studied by means of Nikon-LV150 metallographic microscope. The average grain size was estimated as 15 μm. The microstructure of NiTi specimens for three different magnification is depicted in Figure 2.1.
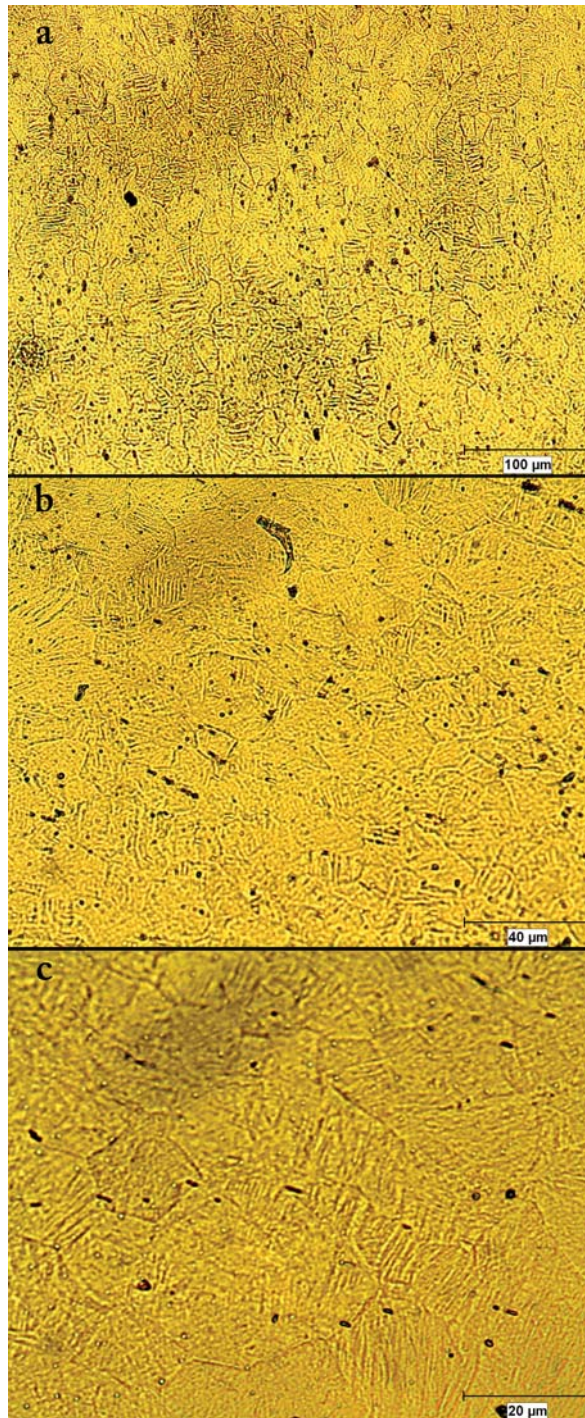
Figure 2.1. Micrograph of NiTi alloy: (a) 20X, (b) 50X, (c) 100X.

2.2. Tensile Testing

Uniaxial tensile tests were carried out with two types of flat dog-bone tensile test specimens. To obtain the material properties in both rolling direction (RD) and transverse direction (TD), the samples were cut in two different directions using electrical discharge machining (EDM). Figure 2.2 illustrates these directions on the NiTi sheet after EDM.
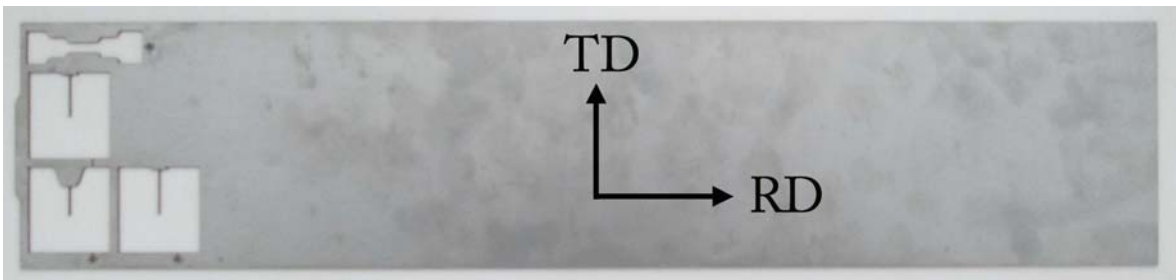
Figure 2.2. Illustration of rolling and transverse directions on NiTi sheet after EDM.

Moreover, since there were different types of tests rigs (servo-hydraulic and screw-driven) with different loading capacities (2 KN, 10 KN, 100 KN), the tensile specimen were cut in two different dimensions. Larger specimens were used in high capacity test rigs and smaller specimens were tested in low capacity machine. The nominal dimensions and optical image of NiTi tensile specimen in transverse and rolling directions are given in Figures 2.3 and 2.4 respectively. ASTM standards E8/E8M-11(Standard Test Methods for Tension Testing of Metallic Materials) [40] and F2516-07 (Standard Test Method for Tension Testing of Nickel-Titanium Superelastic Materials) [41], were used for specimen geometry and test procedure.

The first series of tensile tests were carried out at room temperature using the tensile specimen shown in Figure 2.4. End tabs were used to prevent sliding. The end tabs were fabricated from 2 mm thick Alclad Aluminum 7075-T651 sheets and Araldite 2011 epoxy adhesive was used for bonding between the specimen and end tabs as shown in Figure 2.5.
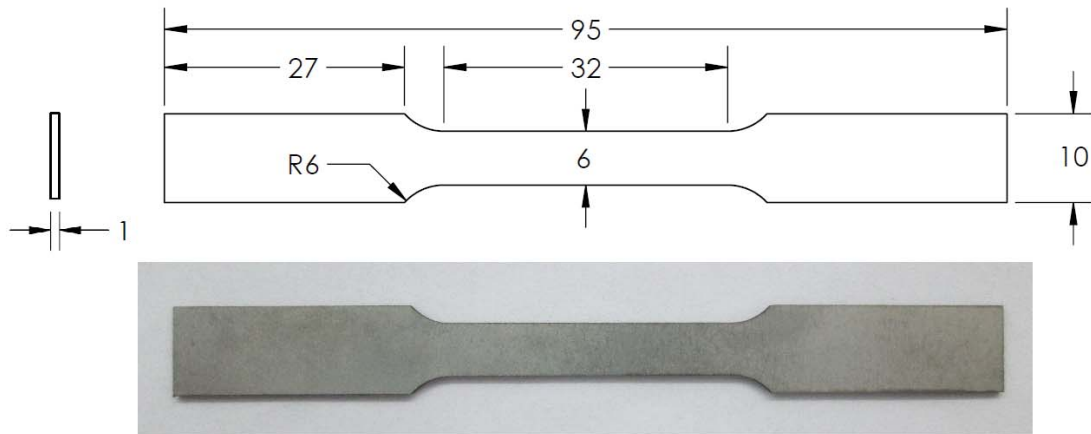
Figure 2.3. Nominal dimensions of NiTi tensile test specimen in transverse direction.
Dimensions in mm.
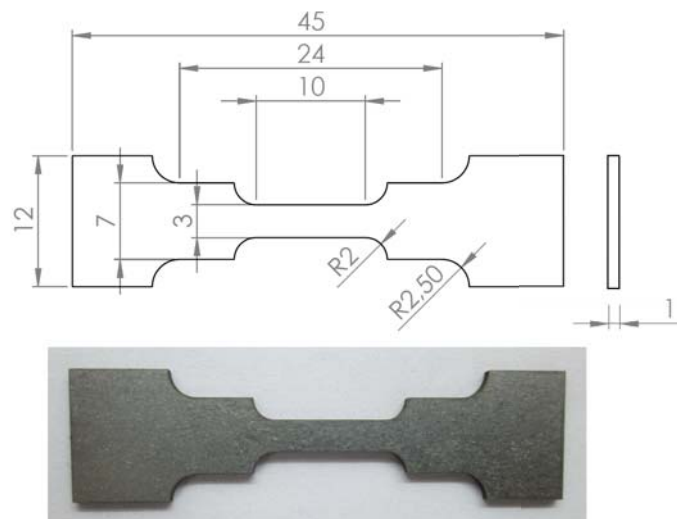
Figure 2.4. Nominal dimensions of NiTi tensile test specimen in rolling direction.
Dimensions in mm.

Figure 2.5. NiTi tensile test specimen with end tabs.

Uniaxial tensile tests were conducted on a computer-controlled screw-driven microtester (INSTRON-5848) with a 2 KN load cell and pneumatic grips. An extensometer was used to measure the strain in longitudinal direction. Figure 2.6 shows the experimental setup.
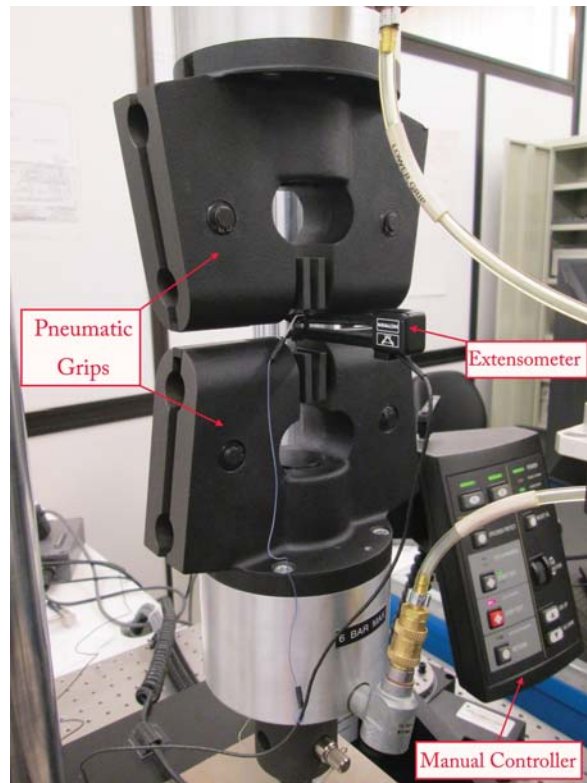
Figure 2.6. INSTRON-5848 setup used for tension tests at room temperature.

The tension tests were performed under displacement control. According to ASTM F2516-07, the material should be pulled to 6% strain with a loading rate of 0.5 mm/min, then unloaded to less than 7 MPa with the same rate, and then pulled to failure with a loading rate of 5 mm/min. However, since the capacity of the microtester

was limited to 2 KN, the second stage of the test i.e. pulling to the failure could not be fulfilled and as a result the specimens were pulled to the maximum capacity of the test rig. Three tensile tests were conducted on samples which were cut parallel to the rolling direction (RD) to assure repeatability of results within experimental error. The stress-strain curves of these three specimens are shown in Figure 2.7, Figure 2.8 and Figure 2.9.
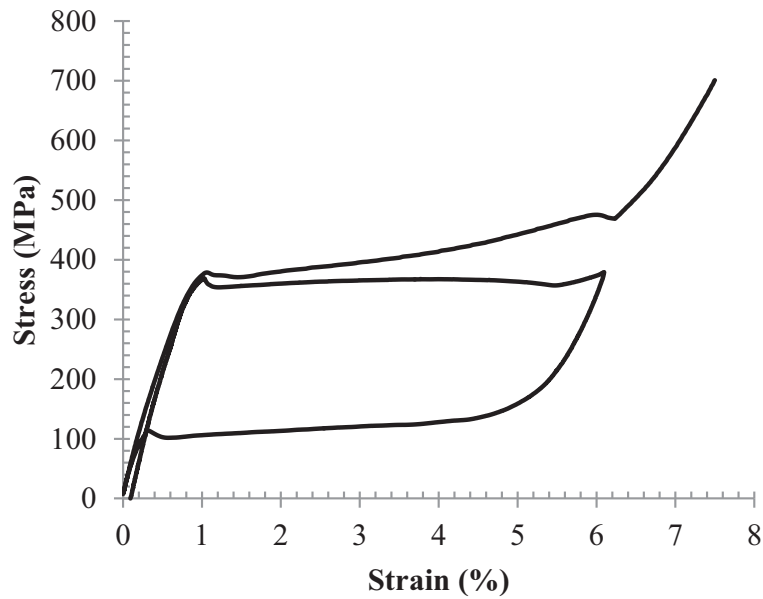
Figure 2.7. Stress-strain curve obtained from first test on INSTRON-5848 at room temperature using NiTi tensile specimen cut parallel to the RD, with a loading rate of 0.5 mm/min during first stage and 5 mm/min during second stage.

In all three tests, the material was fully austenite at the beginning. As the specimen was pulled with a loading rate of 0.5 mm/min, the austenite was elastically loaded with an approximate modulus of 45 GPa. The deviation from linearity began around a stress of 400 MPa and strain of 1%. From this point on, the stress remained almost constant while the strain increased up to almost 6% which was an indication of the forward phase transformation. At 6% strain, the specimen was fully martensite and was unloaded. The unloading followed a similar pattern to the loading. During unloading, the reverse phase transformation started around a stress of 200 MPa. After

Figure 2.8. Stress-strain curve obtained from second test on INSTRON-5848 at room temperature using NiTi tensile specimen cut parallel to the RD, with a loading rate of 0.5 mm/min during first stage and 5 mm/min during second stage.
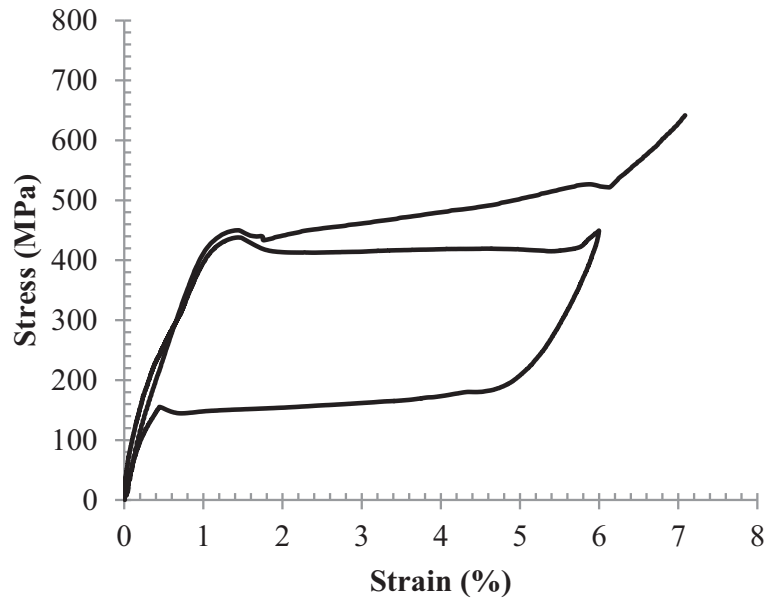
Figure 2.9. Stress-strain curve obtained from third test on INSTRON-5848 at room temperature using NiTi tensile specimen cut parallel to the RD, with a loading rate of 0.5 mm/min during first stage and 5 mm/min during second stage.

the reverse transformation was completed, the austenite was elastically unloaded to 7 MPa with a small amount of residual strain. Afterwards, the second stage of loading started with a loading rate of 5 mm/min. The forward phase transformation started at similar stress and strain values as those of the previous stage. This time however, the stress was not constant during transformation as a result of the increased loading rate, as expected. As a consequence, the forward phase transformation finished around 500 MPa. From this point on, the fully transformed martensite was loaded elastically with an approximate modulus of 14 GPa up to the maximum loading capacity of the test rig i.e. around 700 MPa. The mechanical properties obtained from stress-strain behavior of the NiTi are reported in Table 2.3.

Table 2.3. Mechanical properties obtained from tension tests at room temperature using NiTi specimens cut parallel to RD.

	E_A (GPa)	E_M (GPa)	ϵ^L (%)	UPS (MPa)	LPS (MPa)
Test 1	45	13	5	365	117
Test 2	41	14	5	416	156
Test 3	45	13	5	414	158

As can be seen from Table 2.3, the values of the modulus of elasticity for martensite are smaller than those for austenite. It is important to emphasize that the elastic modulus obtained from the stress-strain curve does not represent the true modulus of martensite (according to some studies it is much higher than that of austenite [42]). In fact, in addition to the elastic deformation of martensite, other deformation mechanisms are operative. In other words, the deformation in the martensite portion of the stress-strain curve is actually a mixed process of elastic deformation of stress induced martensite, plastic deformation of austenite, grain reorientation and detwinning of martensite variants [43]. For measuring the true elastic modulus of martensite other techniques such as neutron diffraction measurements should be used, that is not covered in the present work. As a result, the elastic modulus measurements in this study are based on the macroscopic stress-strain response of the material , and the slope

of the curve for both the austenite and fully transformed martensite is used for the determining the elastic modulus.

According to ASTM F2516-07 [41] , the upper plateau strength (UPS) is determined as the value of the stress at a strain of 3.0% during the initial loading of the specimen. In a similar way, the lower plateau strength (LPS) is determined as the value of the stress at a strain of 2.5% during the unloading of the specimen.

The second series of tensile tests were carried out at room temperature using the tensile specimen shown in Figure 2.3. Again end tabs were used on the specimens to prevent sliding using same material and adhesive as used before. Uniaxial tensile tests were conducted on a computer-controlled screw-driven Zwick/Roel Z010 with a 10 KN load cell and wedge grips. Figure 2.10 shows the experimental setup.
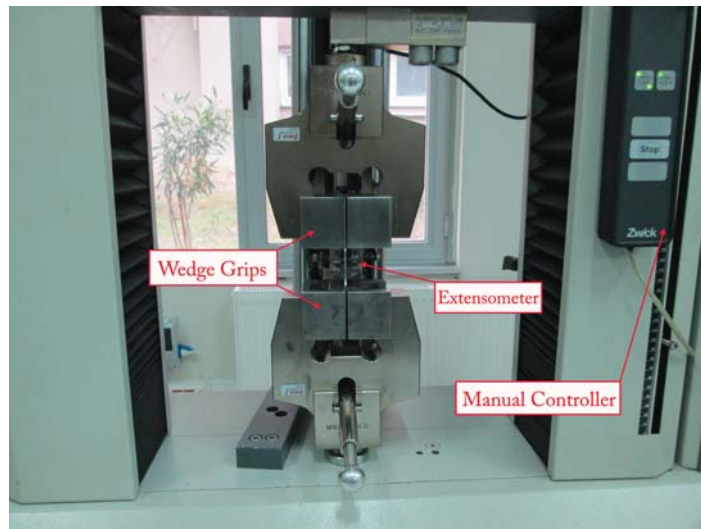
Figure 2.10. Zwick/Roel-Z010 setup used for tension tests at room temperature .

Similar to the previous tests, the material was pulled to 6% strain with a loading rate of 0.5 mm/min, then unloaded to less than 7 MPa with the same rate, and then pulled to failure with a loading rate of 5 mm/min. Here, in the second stage of loading, the specimen was pulled up to 1000 MPa because the epoxy adhesive could not sustain more loads. As a result, pulling to failure could not be fulfilled again. Two tests

were conducted on samples which were cut parallel to the transverse direction (TD) to assure repeatability of results within experimental error. The stress-strain curves of these two specimens are shown in Figures 2.11 and 2.12.
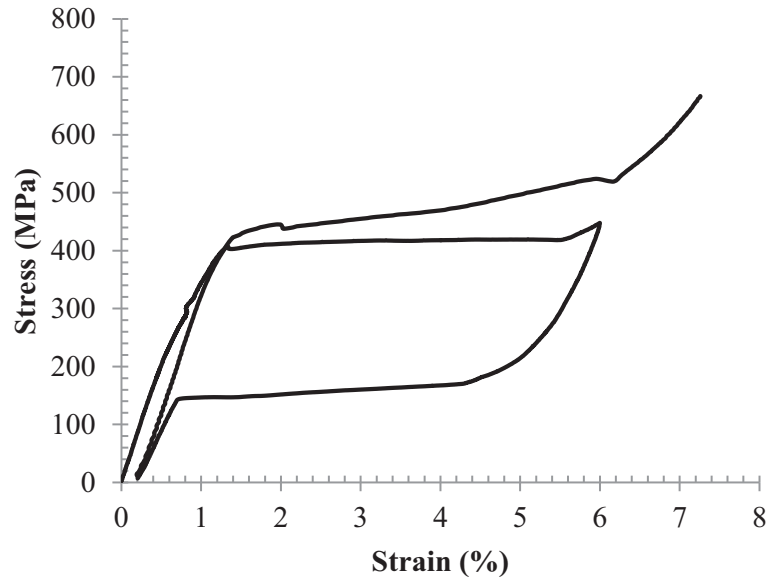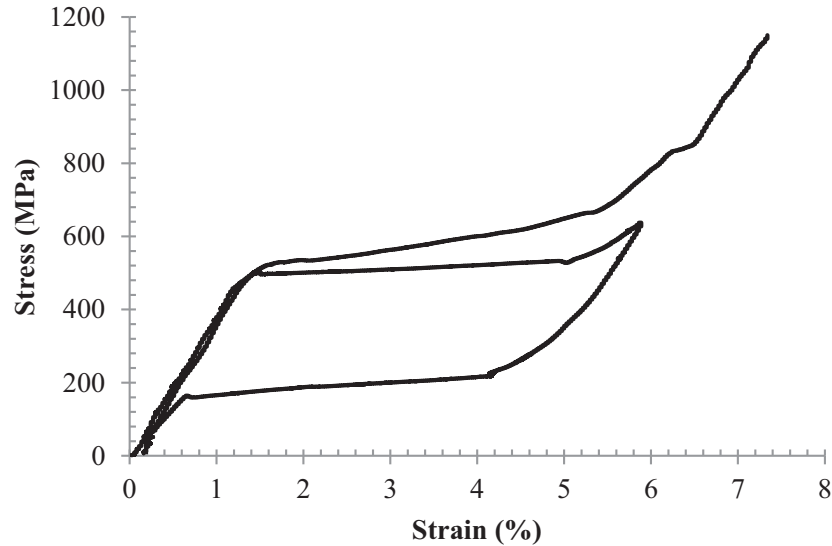

Figure 2.11. Stress-strain curve obtained from first test on Zwick/Roel Z010 at room temperature using NiTi tensile specimen cut parallel to the TD, with a loading rate of 0.5 mm/min during first stage and 5 mm/min during second stage.

In these tests, the specimen, which was initially in the austenite state, was pulled with a loading rate of 0.5 mm/min. The austenite was elastically loaded with an approximate modulus of 38 GPa which was lower than that of the specimens which were pulled along RD. Upon further loading, the phase transformation started around 500 MPa. Stress remained almost constant while strain increased up to 6%. At this point the stress induced martensite was unloaded. Unloading followed a similar pattern. During unloading, the reverse phase transformation started around 200 MPa. After the reverse transformation finished, austenite was elastically unloaded to 7 MPa with a small amount of residual strain. The second stage of loading began with a loading rate of 5 mm/min. The forward phase transformation started at a similar stress and strain values as those of the previous stage. This time however, the stress was not constant during the transformation due to the increased loading rate, as expected. As
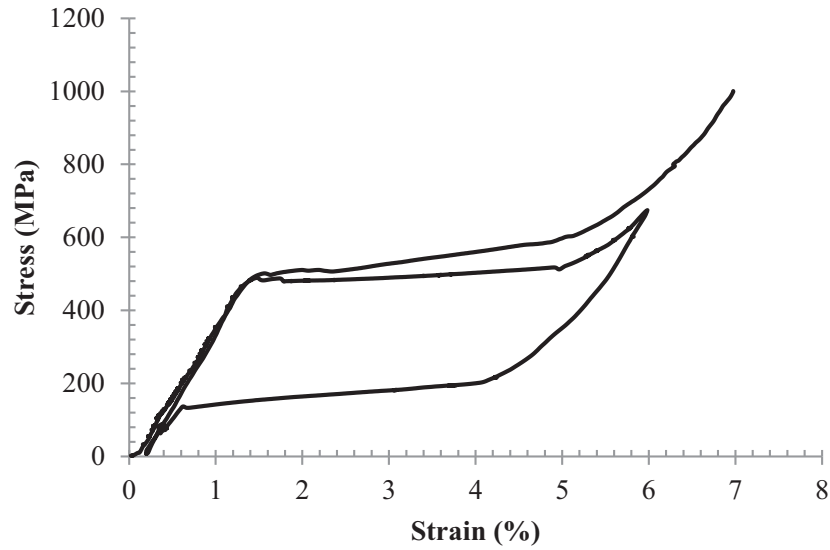
Figure 2.12. Stress-strain curve obtained from second test on Zwick/Roel Z010 at room temperature using NiTi tensile specimen cut parallel to the TD, with a loading rate of 0.5 mm/min during first stage and 5 mm/min during second stage.

a consequence, the forward phase transformation was completed at higher value of stress around 700 MPa. From this point, the stress induced martensite was loaded elastically with an approximate modulus of 34 GPa (which was higher than that of the specimens which were pulled along RD) up to 1000 MPa. The mechanical properties obtained from the stress-strain behavior of the NiTi are reported in Table 2.4.

Table 2.4. Mechanical properties obtained from tension tests at room temperature using NiTi specimens cut parallel to TD.

	E_A (GPa)	E_M (GPa)	ϵ^L (%)	UPS (MPa)	LPS (MPa)
Test 1	38	34	4	508	192
Test 2	38	34	4	489	172

According to the fact that the failure stresses of NiTi could not be obtained in the previous tests due to problems associated with the adhesive or capacity of the test

rig, another tensile test were carried out to overcome the problems encountered. This time a servo-hydraulic test machine (INSTRON-8801) with a 100 KN load cell was used. Consequently, the capacity problem was solved. In addition, the wedge grips of the test machine eliminated need of end tabs. A difficulty in using this test rig was that the test in low rates (lower than 3 mm/min) couldn't be done. Since the second stage of loading i.e. the loading to failure, is conducted with a rate of 5 mm/min, this problem did not affect the procedure. The experimental setup is shown in Figure 2.13.
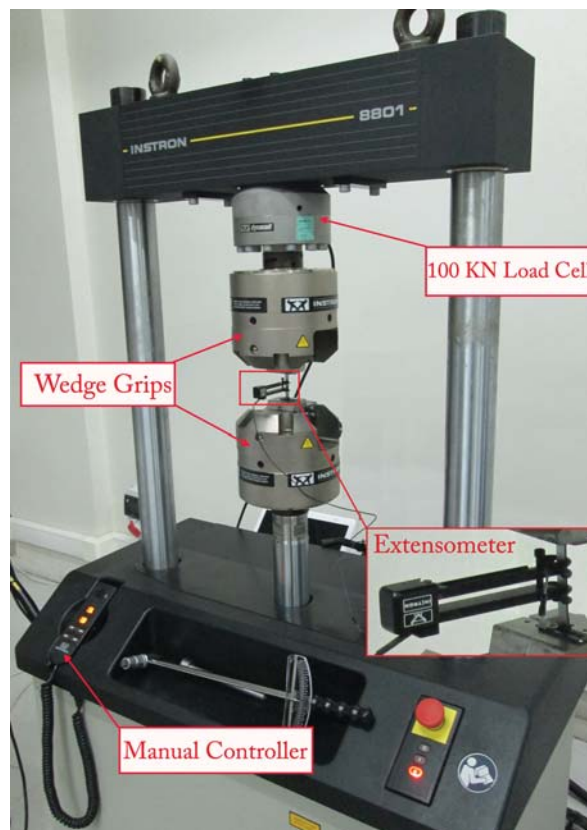
Figure 2.13. INSTRON-8801 experimental setup used for tension tests at room temperature.

As mentioned earlier, the tensile samples, which were cut along the transverse direction (TD) were pulled to failure with a loading rate of 5 mm/min. The obtained stress-strain curve is shown in Figure 2.14.
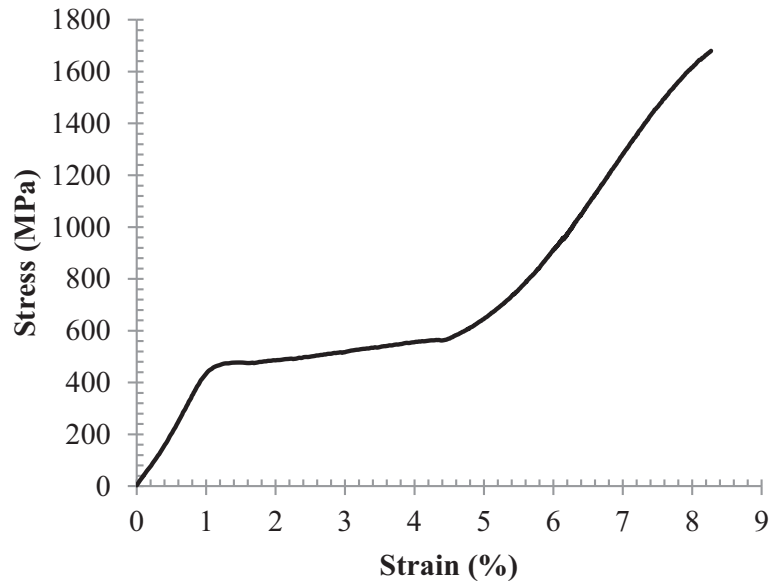
Figure 2.14. Stress-strain curve obtained from test on INSTRON-8801 at room temperature to measure σ_{UTS} using NiTi tensile specimen cut parallel to the TD, with a loading rate of 5 mm/min.

In this test, the austenite was elastically loaded with an approximate modulus of 48 GPa. The phase transformation started around 400 MPa and at a strain of 1%. As a result of high loading rate, the stress plateau had a slope. The forward phase transformation finished at around 700 MPa. From this point on, the stress induced martensite was loaded elastically with an approximate modulus of 38 GPa. Upon further loading the failure occured. As can be seen in Figure 2.14, no specific yield point is observed in the stress-strain behavior of the material. As a result, only the ultimate tensile stress (σ_{UTS}) can be measured. The mechanical properties obtained from the stress-strain behavior of the NiTi are tabulated in Table 2.5.

Uniaxial tensile tests were also carried out at $100\,°C$ to observe the behavior above martensite desist temperature M_d (the temperature above which the stress induced phase transformation is suppressed). Loading and unloading tests with a rate of 3 mm/min on the superelastic NiTi specimens which were cut parallel to transverse di-

Table 2.5. Mechanical properties obtained from tension tests at room temperature using NiTi specimens cut parallel to TD.

	E_A (GPa)	E_M(GPa)	ϵ^L (%)	σ_{UTS} (MPa)
Test 1	48	38	4	1680

rection (Figure 2.3), were performed at $100\,°C$ using INSTRON-8801. A hot air blower was used to increase the specimen temperature. During the test, the temperature was measured by means of Optris-PI infrared thermometer. The reflection from the specimen surface was prevented by means of a black matt paint to make sure that the temperature measurements were reliable. The experimental setup is shown in Figure 2.15. Two tests were carried out to assure repeatability of results within experimental error. The stress-strain curves are shown in Figure 2.16.
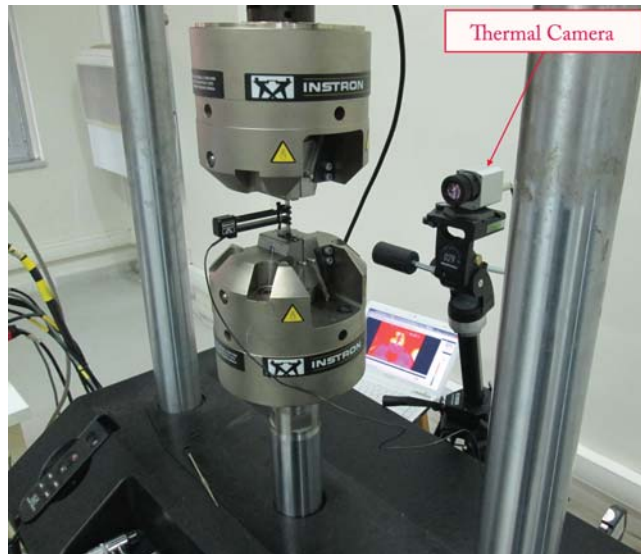
Figure 2.15. INSTRON-8801 experimental setup used for tension tests at high temperature.

The stress-strain curves illustrates that the reversibility due to phase transformation during unloading is not observed anymore. Consequently, the irreversible strain
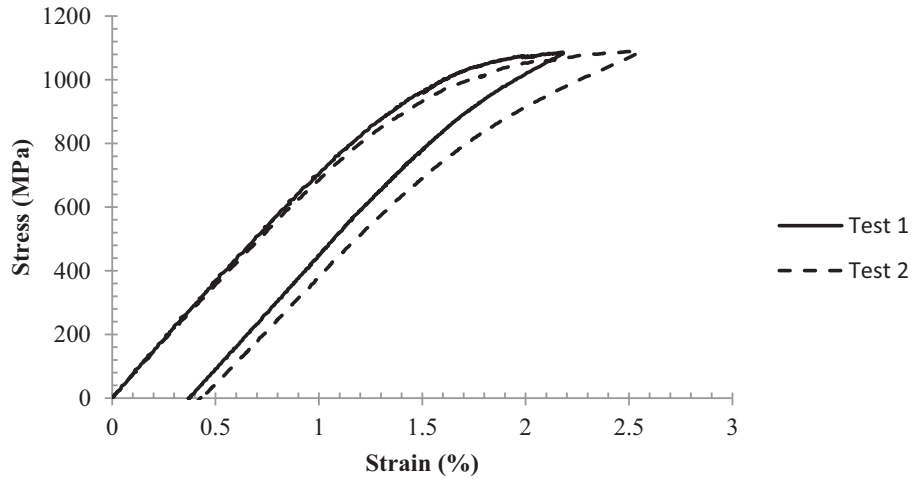
Figure 2.16. Stress-strain curves obtained from tests on INSTRON-8801 at 100 °C using NiTi tensile specimen cut parallel to the TD, with a loading rate of 3 mm/min.

reflects the plastic deformation of austenite. The elastic modulus of austenite in both tests at high temperature were found to be 70 GPa, a value much larger than that of austenite at room temperature. It indicates that the change of elastic modulus of NiTi is very different from conventional metals in which the elastic modulus decreases as the temperature increases. Finally, to obtain the ultimate tensile stress (σ_{UTS}) of NiTi at high temperature, another tension test was performed using same specimen, configuration and procedure as previous tensile tests at high temperature. In this test, however, the specimen was pulled to failure as illustrated in Figure 2.17. The ultimate tensile stress (σ_{UTS}) is found to be 1262 GPa which is smaller than that of specimens tested at room temperature as expected.
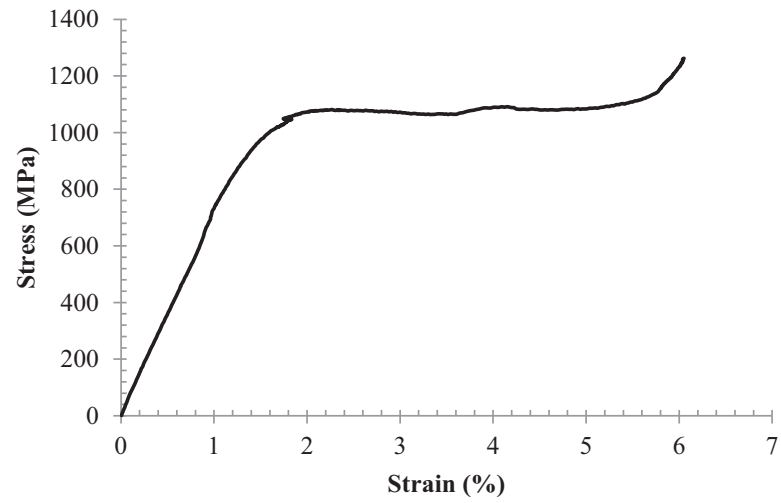
Figure 2.17. Stress-strain curve obtained from test on INSTRON-8801 at $100\,^{\circ}$C to measure σ_{UTS} using NiTi tensile specimen cut parallel to the TD, with a loading rate of 5 mm/min.

3. EXPERIMENTAL INVESTIGATION OF FRACTURE BEHAVIOR

A crack can be loaded in the three different modes. Mode-I or the opening mode is caused by tension. However, Mode-II (sliding mode) and the Mode-III (tearing mode) are caused by in-plane and out-of-plane shearing, respectively. Mode-I is the predominant mode in majority of fracture problems in engineering so the present study is limited to this case.

3.1. Stress Intensity Factor

3.1.1. Basics

For describing the stresses ahead of the crack, a polar coordinate system is defined with the origin at the crack tip as shown in Figure 3.1.
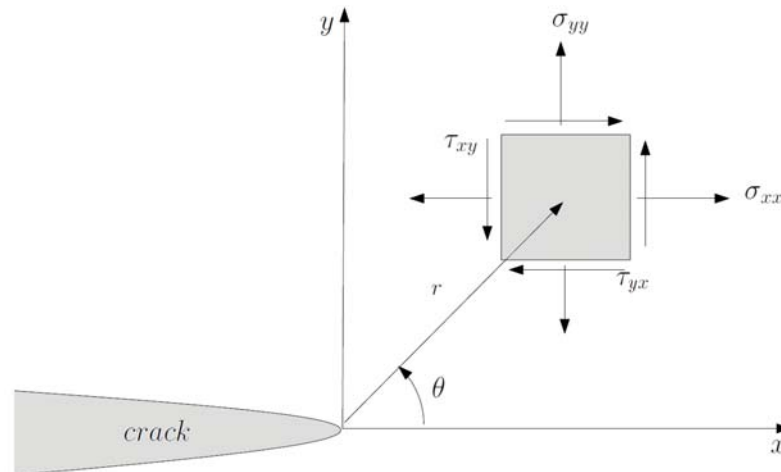
Figure 3.1. Definition of the coordinate system ahead of the crack tip [44].

The stress components near the crack tip, in linear elastic isotropic material for Mode-I loading are:

$$\sigma_{xx} = \frac{K_I}{\sqrt{2\pi r}} \cos\left(\frac{\theta}{2}\right) \left[1 - \sin\left(\frac{\theta}{2}\right) \sin\left(\frac{3\theta}{2}\right)\right] + ... \tag{3.1a}$$

$$\sigma_{yy} = \frac{K_I}{\sqrt{2\pi r}} \cos\left(\frac{\theta}{2}\right) \left[1 + \sin\left(\frac{\theta}{2}\right) \sin\left(\frac{3\theta}{2}\right)\right] + ... \tag{3.1b}$$

$$\tau_{xy} = \frac{K_I}{\sqrt{2\pi r}} \cos\left(\frac{\theta}{2}\right) \sin\left(\frac{\theta}{2}\right) \cos\left(\frac{3\theta}{2}\right) + ... \tag{3.1c}$$

$$\sigma_{zz} = 0 \qquad \text{(plane stress)} \tag{3.1d}$$

$$\sigma_{zz} = \nu(\sigma_{xx} + \sigma_{yy}) \qquad \text{(plane strain)} \tag{3.1e}$$

$$\tau_{xz} = \tau_{yz} = 0. \tag{3.1f}$$

It is worth mentioning that these equations are derived based on the theory of linear elasticity and higher order terms are ignored. Because the nonzero stress components rapidly increase near the crack tip. Stresses tend to infinity upon approaching the crack tip because of the $\frac{1}{\sqrt{r}}$ singularity. Since all the nonzero stresses are proportional to the quantity K_I, the crack tip stress field can be described by this factor which is called stress intensity factor. The stress intensity factor is given a subscript to denote the mode of loading. It is an extremely important fracture mechanics parameter which measures the severity of the crack:

$$K_I = \lim_{r,\theta \to 0} \left(\sigma_{yy} \sqrt{2\pi r}\right). \tag{3.2}$$

In finding K, the material is assumed to be linear elastic and that the approach being used is called linear elastic fracture mechanics (LEFM) [45]. It is generally convenient to express K as a function of applied stress and crack length by the following equation:

$$K = f\sigma\sqrt{\pi a} , \tag{3.3}$$

where a is the crack length, σ is the remote stress and the quantity f is a dimensionless function that depends on the geometry and loading configuration. For the compact

tension (CT) specimen, K is calculated using the following equation:

$$K = \frac{P}{B\sqrt{W}} \ f\left(\frac{a}{W}\right), \tag{3.4}$$

where:

$$f\left(\frac{a}{W}\right) = \frac{2 + \left(\frac{a}{W}\right)\left[0.886 + 4.64\left(\frac{a}{W}\right) - 13.32\left(\frac{a}{W}\right)^2 + 14.72\left(\frac{a}{W}\right)^3 - 5.6\left(\frac{a}{W}\right)^4\right]}{\left(1 - \frac{a}{W}\right)^{\frac{3}{2}}}, \tag{3.5}$$

for which P is the applied load, B is the specimen thickness and W is the specimen width as shown in Figure 3.2.
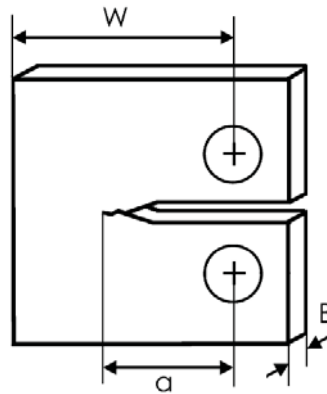
Figure 3.2. Schematic of CT specimen.

As long as this K is below a critical value, the structure can resist a crack. This critical value is called the fracture toughness (K_C). The values of K_C are affected by some parameters such as thickness, temperature and loading rate. As shown in Figure 3.3, K_C decreases with increasing thickness until a plateau is reached. From this point on, K_C is no longer affected by further increase in thickness and it becomes relatively constant. This value is denoted as K_{IC} and is called the plain strain fracture toughness.
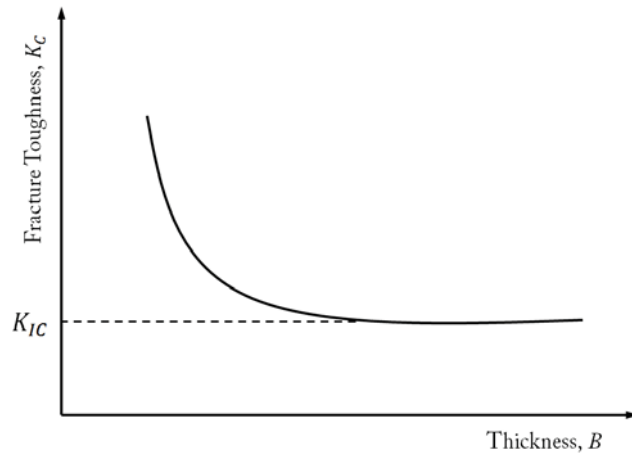
Figure 3.3. Schematic representation for dependence of K_C on Thickness.

3.1.2. Experiments

In fracture toughness K_C testing, an increasing displacement is applied to a cracked specimen until it breaks. Load versus displacement is recorded during the test; K_C is determined using the maximum load which is recorded from load-displacement curve and the specimen geometry i.e. the crack length, specimen width and thickness. Fracture toughness K_C testing of metals based on LEFM principles is governed by ASTM E399-12 (Standard Test Method for Linear-Elastic Plane-Strain Fracture Toughness K_{IC} of Metallic Materials) [46].

K_C tests were carried out using NiTi compact tension (CT) specimens. CT specimens were cut by means of electro discharge machining (EDM) from 1 mm thick such that the loading direction was parallel to rolling direction (RD). ASTM E399-12 [46] were used for specimen geometry and test procedure. It is important to note that some of conditions and limitations given by the standard test method such as specimen thickness were not applied because of the thickness of the NiTi sheet used. NiTi alloys are normally not used as a bulk material, and consequently, they are commercially available in the shape of wires, thin sheets and tubes [38]. Nominal dimensions and optical image of CT specimen are given in Figure 3.4.
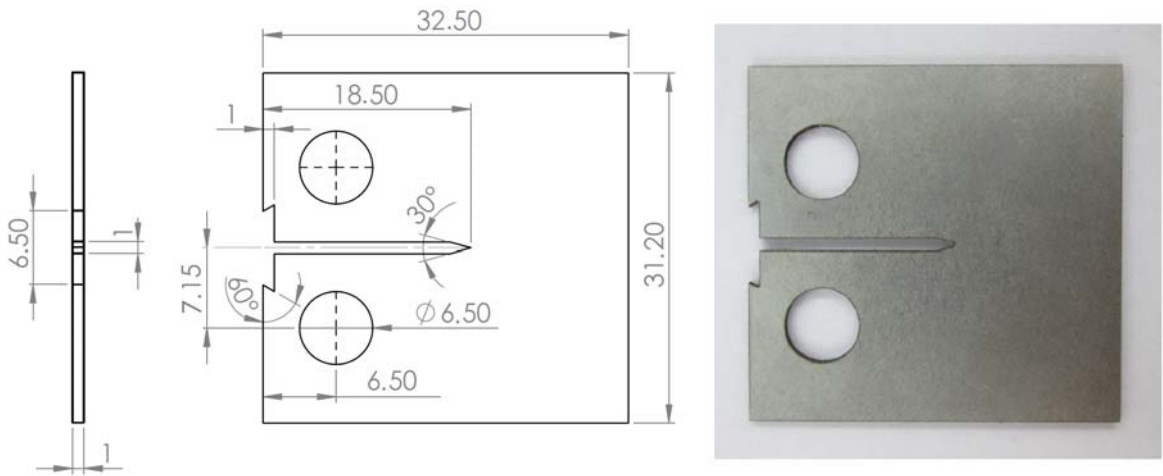
Figure 3.4. Nominal dimensions of NiTi compact tension (CT) specimen used in K_C testing. Dimensions in mm.

Considering the fact that even the narrowest practical machined notch cannot simulate a natural crack [46], all specimens were fatigue pre-cracked under cyclic loading, to produce an ideally sharp crack. The fatigue pre-cracking was carried out at room temperature using the servo-hydraulic INSTRON-8801 test rig with a 100 KN load cell. The experimental setup for fatigue pre-cracking is shown in Figure 3.5.

The standard method suggests that the pre-crack load be selected such that the maximum stress intensity factor during fatigue crack growth does not exceed 80% of the estimated K_{IC} value of the material. Using available K_{IC} measurements reported in literature, the maximum load associated with the 80% of K_{IC} was estimated around 450 N. To decrease the failure possibility during fatigue, the maximum pre-cracking load for the NiTi CT specimens was selected as 300 N which was later decreased to 200 N . It should be noted that the pre-cracking was performed using INSTRON-SAX software in load control mode with sinusoidal wave form at a frequency of 5 Hz . Different crack lengths were obtained (13.5 mm $< a <$ 14.3 mm) which were within the range of ASTM E399 ($0.45W < a < 0.55W$). Table 3.1 shows the details of fatigue pre-cracking of NiTi CT specimens for K_C testing.
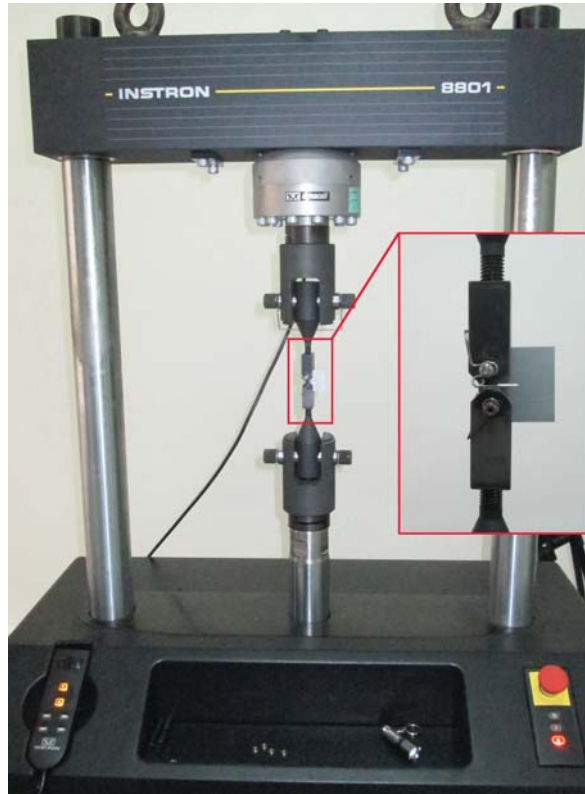
Figure 3.5. INSTRON-8801 experimental setup used for fatigue pre-cracking of NiTi CT specimens.

Table 3.1. Details of fatigue pre-cracking of NiTi CT specimens for K_C testing.

	Load(N)	Cycle	Frequency (Hz)	Pre-crack Size (mm)
Specimen 1	300	2500	5	1.5
Specimen 2	300	2500	5	1.7
Specimen 3	200	10000	5	2.3
Specimen 4	200	10000	5	2.3

The optical images of pre-cracks on four specimens are shown in Figure 3.6. It is worth noting that the exact measurement of pre-crack sizes was carried out after final fracture using the OLYMPUS 100AL optical microscopy.
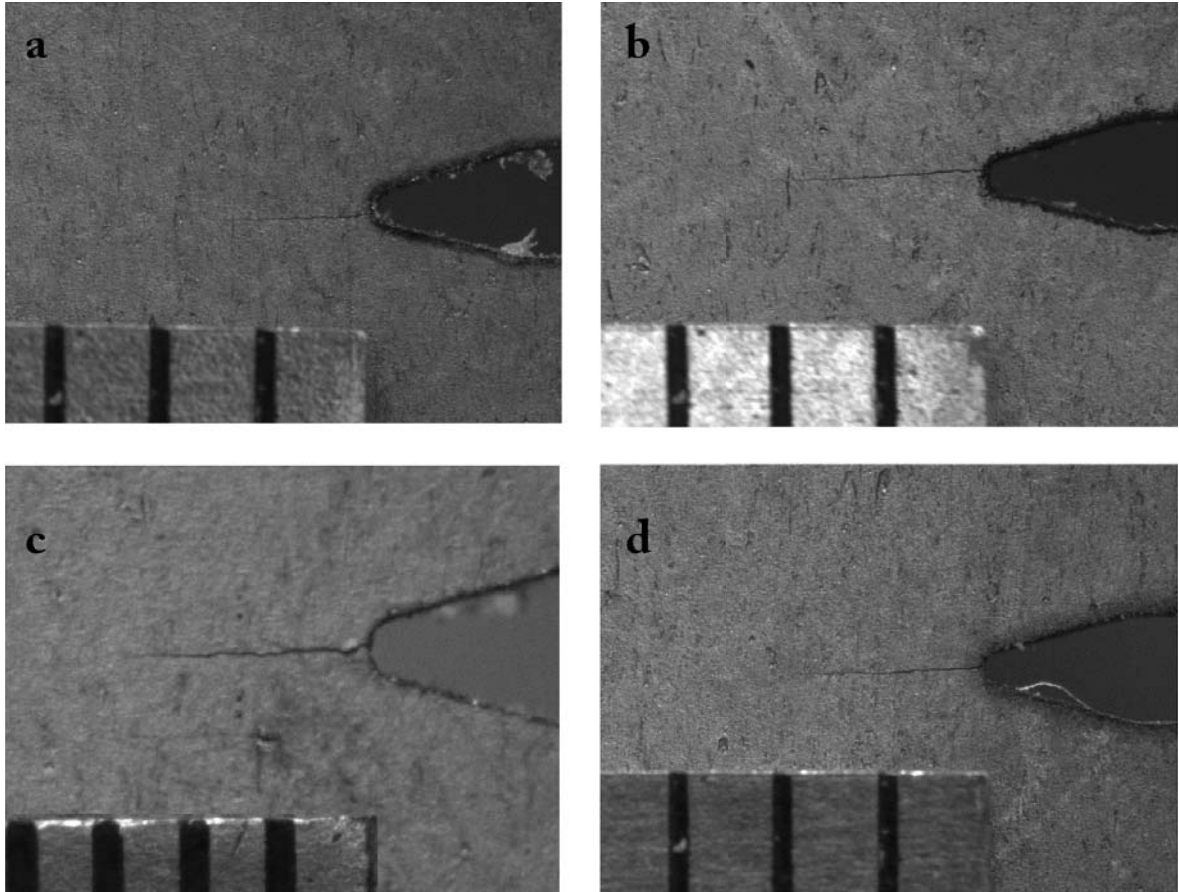
Figure 3.6. Optical images of pre-cracks on NiTi CT specimens used in K_C testing; (a) specimen 1, (b) specimen 2, (c) specimen 3, and (d) specimen 4.

According to ASTM E399-12 [46], to maintain a quasi-static loading condition, the specimen should be loaded such that the rate of increase of stress intensity factor $(\dot{K})$, is between 0.55 and 2.75 MPa$\sqrt{\text{m}}$/s. The testing machine loading rate $(\dot{\Delta}_{LL})$ associated with this allowable range was determined using ASTM E1921-13 [47], as a function of E, $\dot{K}$ and W for each allowable specimen geometry. Table 3.2 shows the allowable loading rate for different a/W values. Using the mentioned method, the load-line displacement rate was found to be 0.5 mm/min.

Table 3.2. Loading rate estimation for CT specimens [47].

SE(B) Specimen Rate Estimation			CT Specimen Rate Estimation		
a/W	$\frac{t_M \dot{K}}{\sigma_Y \sqrt{W}}$	$\frac{E\dot{\Delta}_{LL}}{\frac{dK}{dt}\sqrt{W}}$	a/W	$\frac{t_M \dot{K}}{\sigma_Y \sqrt{W}}$	$\frac{E\dot{\Delta}_{LL}}{\frac{dK}{dt}\sqrt{W}}$
0.45	0.346	5.064	0.45	0.412	3.475
0.50	0.333	5.263	0.50	0.386	3.829
0.55	0.318	5.522	0.55	0.361	4.212
0.60	0.302	5.851	0.60	0.336	4.635
0.65	0.283	6.267	0.65	0.312	5.118
0.70	0.263	6.798	0.70	0.287	5.696

After fatigue pre-cracking, fracture tests were carried out both at room temperature and high temperature (100 °C). As already mentioned, mechanical tests above the martensite desist temperature M_d, were used to observe mechanical properties of austenite in the absence of martensitic transformation. Consequently, by comparing the values of K_C obtained from these two temperatures, one would be able to discuss the effect of stress induced martensitic transformation occurring at the crack tip of NiTi specimens. Fracture tests were carried using the screw-driven INSTRON-5848 test machine with a 2 KN load cell. A COD gauge was used to measure the displacement at the crack mouth. The experimental setup is shown in Figure 3.7.

The tests were performed in displacement control mode with a loading rate of 0.5 mm/min. Load versus crack mouth opening displacement was recorded. Bluehill software was used to control the test procedure and record the data. A hot air blower was employed to increase the specimen temperature for high temperature tests. During the test, the temperature of the specimen was measured by means of Optris-PI infrared thermometer and the reflection from the specimen surface was prevented by means of a black matt paint to increase the temperature measurement accuracy. The infrared thermometer output in two temperature values is shown in Figure 3.8. The CT specimens were then pulled to fracture.
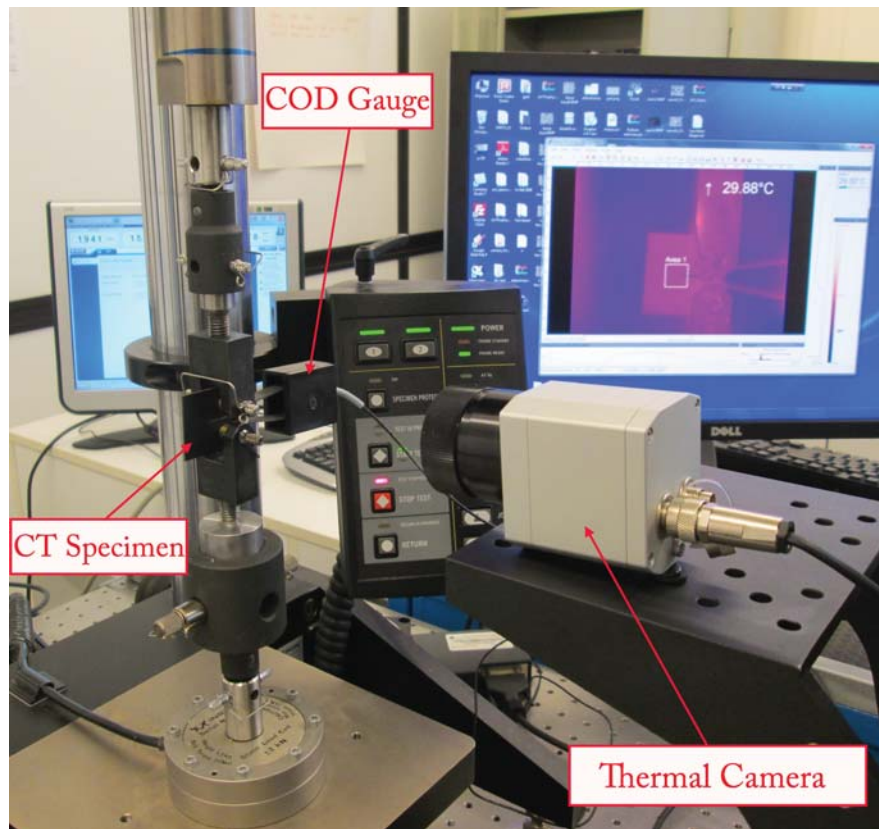
Figure 3.7. INSTRON-5848 experimental setup used for K_C determination of NiTi CT specimens.
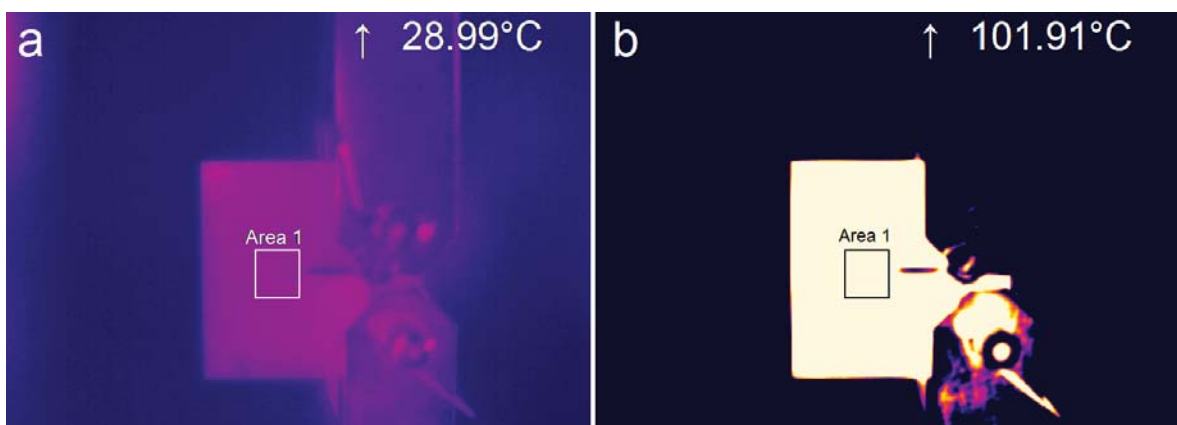
Figure 3.8. Infrared thermometer output at: (a) room temperature, (b) high temperature.

3.1.3. Results and Discussion

Two tests were carried out at each temperature to assure repeatability of results within experimental error limits. The Load-CMOD curves obtained from fracture tests on NiTi CT specimens at room temperature are shown in Figures 3.9 and 3.10. It should be noted that two different crack sizes were used to discuss the effect of crack size on fracture toughness.
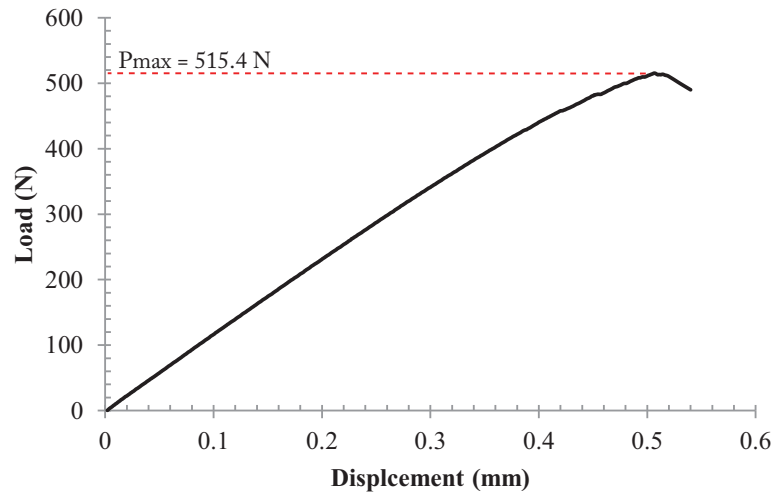
Figure 3.9. Load-CMOD curve for NiTi CT specimen with a=13.5 mm at room temperature.

The characteristic features of the load-displacement curves suggested that a deviation from linearity was observed before the maximum load was reached. As expected, the maximum load for the specimen with smaller crack size was higher. K_C values were then obtained using maximum load P_{max} from load-displacement curves and Equation 3.4. The results are tabulated in Table 3.3.

An average value of K_C equal to 31.9 MPa$\sqrt{m}$ was calculated from the tests at room temperature. It is worth noting that this value is very close to previous literature
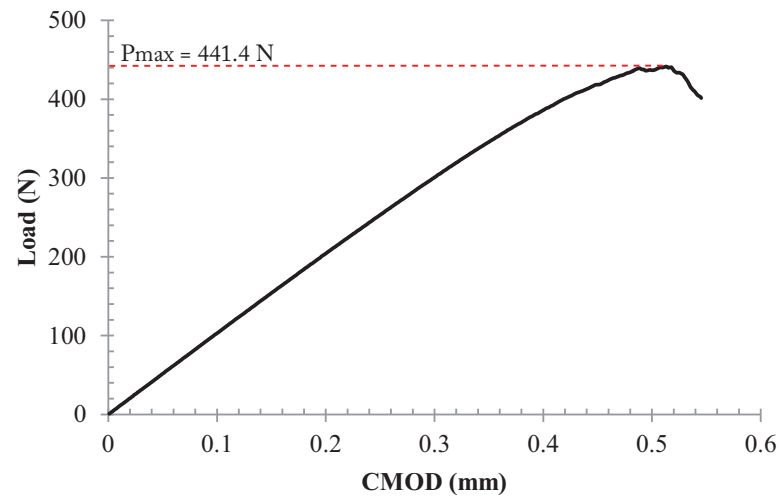
Figure 3.10. Load-CMOD curve for NiTi CT specimen with a=14.3 mm at room temperature.

Table 3.3. Results of K_C testing of NiTi CT specimens at room temperature.

	P_{max} (N)	a (mm)	K_C (MPa$\sqrt{m}$)
Test 1	515.4	13.5	32.8
Test 2	441.4	14.3	31.1

results which indicate average K_C values around 32 MPa$\sqrt{\text{m}}$ [38] and 34 MPa$\sqrt{\text{m}}$ [36] for superelastic NiTi SMA. It can be clearly seen that the K_C is independent of the length of crack. The Load-CMOD curves obtained from fracture tests on NiTi CT specimens at 100 °C are shown in Figures 3.11 and 3.12.
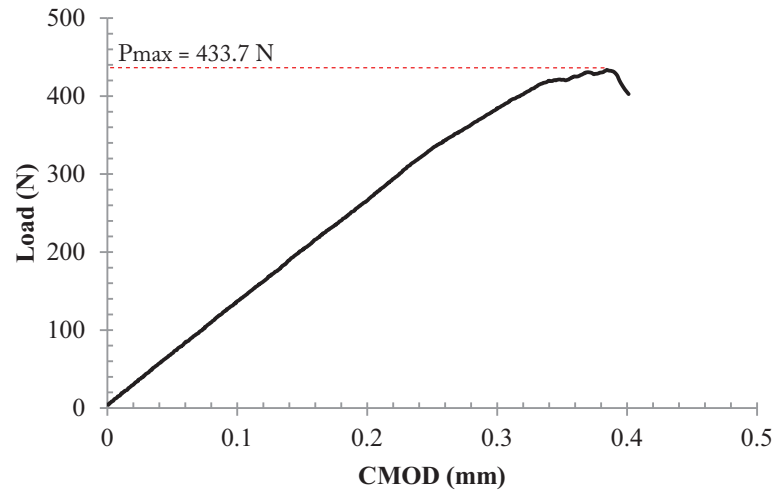
Figure 3.11. Load-CMOD curve for NiTi CT specimen with a=13.7 mm at 100 °C.

Similar to the fracture tests at room temperature, a deviation from linearity was observed before the maximum load was reached. However, this deviation was more considerable in the case of high temperature tests, indicating more stable crack growth in specimens tested at 100 °C. Later observations of fractured samples supported this claim. Similar to previous tests, the specimen with a longer crack fractured at lower load values. K_C values were obtained using a similar approach and the results are tabulated in Table 3.4.

An average value of K_C equal to 28.1 MPa$\sqrt{\text{m}}$ was calculated from the fracture tests at high temperature. The results show that similar to the tests at room temperature, the fracture toughness values are independent of crack size. Stress intensity factor (K) versus crack mouth opening displacement (CMOD) curves for NiTi SMA for different a/W ratios at room temperature and 100 °C are shown in Figure 3.13.
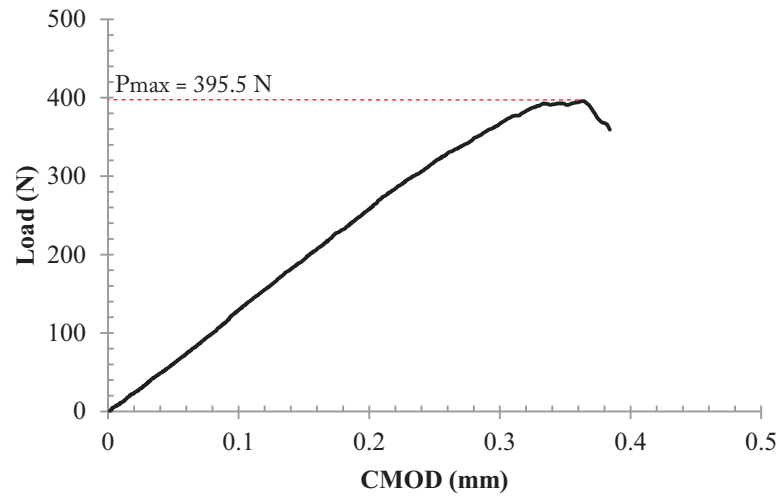
Figure 3.12. Load-CMOD curve for NiTi CT specimen with a=14.3 mm at $100\,°C$.

Table 3.4. Results of K_C testing of NiTi CT specimens at $100\,°C$.

	P_{max} (N)	a (mm)	K_C (MPa$\sqrt{\text{m}}$)
Test 1	433.7	13.7	28.3
Test 2	395.5	14.3	27.9
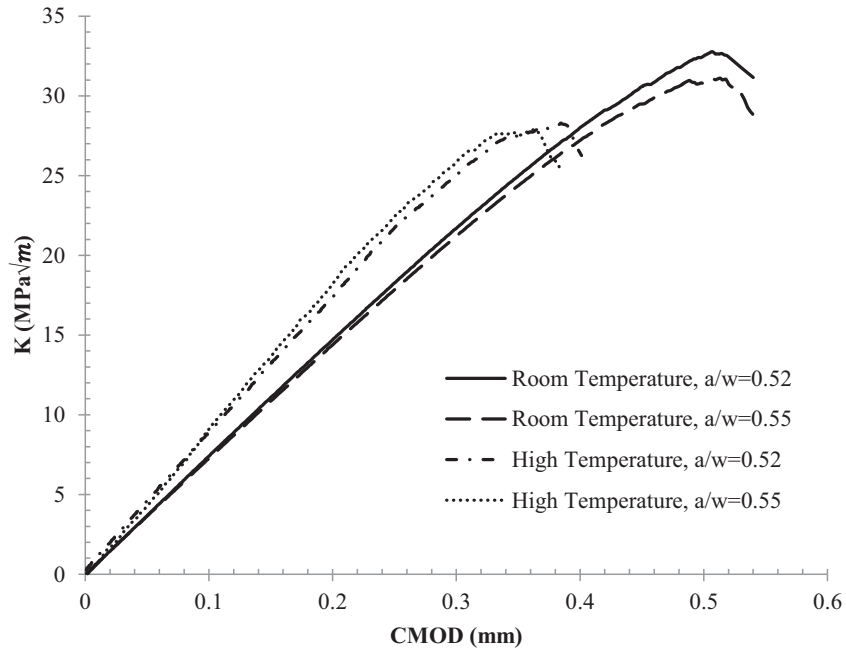
Figure 3.13. Stress intensity factor vs. CMOD curves for NiTi SMA for different a/W ratios at room temperature and at $100\,°C$.

Comparisopn of the results obtained at two different temperature values, clearly shows that increasing the temperature above the martensite desist temperature M_d, decreases K_C of NiTi specimens. In other words, when the stress induced martensite transformation is suppressed at the crack tip, the specimen shows lower resistance to the crack growth which demonstrates the toughening effect of martensite transformation in NiTi SMAs.

3.2. Crack Tip Opening Displacement

3.2.1. Basics

LEFM is valid as long as nonlinear material deformation is confined to a very small region surrounding the crack tip. Elastic plastic fracture mechanics (EPFM) approach is used where LEFM is no longer valid i.e. in the case of nonlinear materials.

Considering the fact that crack blunting occurs in nonlinear materials prior to fracture as shown in Figure 3.14, crack tip opening displacement (CTOD) is defined as a fracture parameter which describes crack tip conditions in these class of materials. Like the stress intensity factor, critical values of CTOD can be used as a measure of fracture toughness.
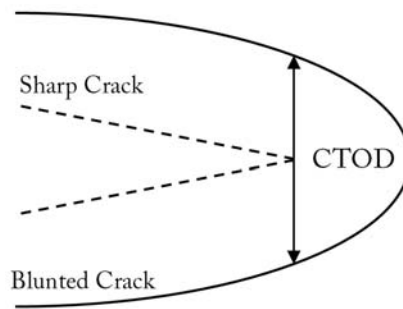
Figure 3.14. Schematic of crack tip blunting resulting in CTOD.

Because the crack opening displacement varies as the crack tip is approached, the definition of CTOD is somewhat arbitrary and depends on distance from the crack tip. Using crack tip displacement field at the physical crack tip, and considering the fact that crack tip plasticity makes the crack behave as if it is slightly longer, Wells [48], found a relationship between CTOD and stress intensity factor K, assuming an effective crack length of $a + r_y$ as shown in Figure 3.15. The crack tip displacement field for Mode-I loading in linear elastic isotropic material is governed by the following equation:

$$u_y = \frac{K_I}{2\mu}\sqrt{\frac{r}{2\pi}}\sin\left(\frac{\theta}{2}\right)\left[\kappa + 1 - 2\cos^2\left(\frac{\theta}{2}\right)\right], \tag{3.6}$$

where K_I is Mode-I stress intensity factor, μ is the shear modulus, r and θ are polar coordinates, $\kappa = (3-\nu)/(1+\nu)$ for plain stress and $\kappa = 3 - 4\nu$ for plain strain , where ν is the Poisson's ratio. Using $\theta = \pi$ and $r = r_y$, the displacement behind the effective crack tip can be obtained as:

$$u_y = \frac{\kappa + 1}{2\mu}K_I\sqrt{\frac{r_y}{2\pi}} = \frac{4}{E'}K_I\sqrt{\frac{r_y}{2\pi}} \ , \tag{3.7}$$
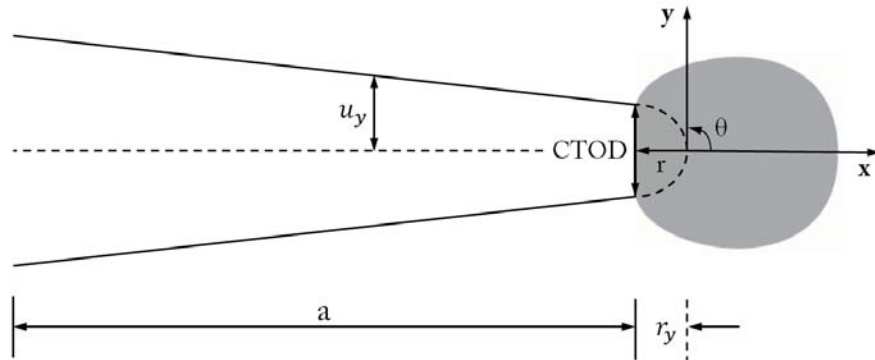
Figure 3.15. Irwin plastic zone correction.

where $E' = E$ for plane stress and $E' = E/(1 - \nu^2)$ for plane strain. r_y (the radius of the plastic zone) for plane stress is:

$$r_y = \frac{1}{2\pi} \left(\frac{K_I}{\sigma_{YS}} \right)^2 , \tag{3.8}$$

where σ_{YS} is the yield stress. Substituting Equation 3.8 into Equation 3.7 gives:

$$CTOD = 2u_y = \frac{4}{\pi} \left(\frac{K_I^2}{\sigma_{YS} E'} \right) . \tag{3.9}$$

Considering the relation between the energy release rate G and stress intensity factor K, $(G = k_I^2/E')$ an alternative relation for $CTOD$ is obtained as:

$$CTOD = \frac{4}{\pi} \left(\frac{G}{\sigma_{YS}} \right) . \tag{3.10}$$

As illustrated in Figure 3.16, using strip yield zone model approach [49], CTOD can also be described as the crack opening displacement at the end of the strip yield zone:

$$CTOD = \frac{K_I^2}{\sigma_{YS} E'} = \frac{G}{\sigma_{YS}} . \tag{3.11}$$

It can be seen the Equation 3.11 is slightly different from Equation 3.10. CTOD can
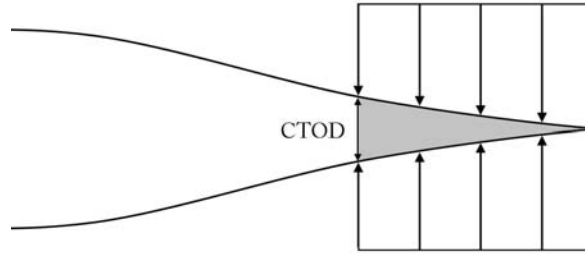
Figure 3.16. Estimation of CTOD from the strip yield model.

be expressed in a general form as follows:

$$CTOD = \frac{K_I^2}{m\sigma_{YS}E'} = \frac{G}{m\sigma_{YS}} \quad , \tag{3.12}$$

where m is a dimensionless constant that depends on the stress state and material properties. $m = 1$ for both linear elastic and elastic-plastic cases based on the strip yield model which assumes plane stress conditions and a non-hardening material. Since $J = G$ for linear elastic material behavior [44]:

$$CTOD = \frac{J}{m\sigma_{YS}} \quad . \tag{3.13}$$

Although this equation describes the relationship between CTOD and J in the limit of small scale yielding, it applies well beyond the validity limits of LEFM [44]. Rice [50], also defined the CTOD as the displacement at the 90° intercept as depicted in Figure 3.17. Shih [51] invoked this definition to obtain a relationship between the J and the CTOD by means of Hutchinson-Rice-Rosengren (HRR) solution:

$$CTOD = \frac{d_n J}{\sigma_{YS}} \quad , \tag{3.14}$$

where the coefficient d_n depends on the material properties. $d_n = 1$ for a non-hardening material in plane stress condition. Comparing Equation 3.14 and Equation 3.13 indicates that $d_n = 1/m$.
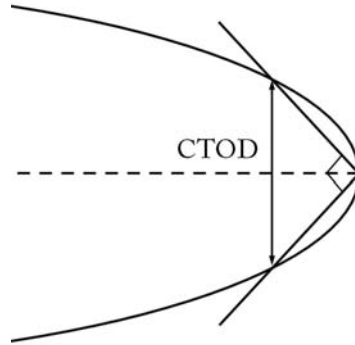
Figure 3.17. Definition of CTOD as the displacement at the intersection of a 90°

vertex with the crack flanks.

3.2.2. Experiments

In laboratory measurements of CTOD, the load line displacement (LLD) is measured and the CTOD is then inferred because its direct measurement is not practical. The CTOD fracture toughness measurement is governed by ASTM E1290-08 (Standard Test Method for Crack Tip Opening Displacement Fracture Toughness Measurement) [52]. In this test method crack tip opening displacement is the displacement of the crack surfaces normal to the crack plane at the tip of the fatigue pre-crack. According to this test method, the determination of CTOD at the onset of unstable brittle crack extension, characterizes the fracture toughness of the material. The test method involves displacement controlled loading of fatigue pre-cracked specimens. Load versus clip gauge crack opening displacement is recorded. Using the obtained load-displacement curve, the CTOD is calculated using the following relationship:

$$CTOD = \left(\frac{1}{m\sigma_Y}\right)\left[\frac{K_I^2}{E'} + \frac{\eta A_p}{B(W-a)}\right], \tag{3.15}$$

where $\sigma_Y = (\sigma_{YS} + \sigma_{UTS})/2$ and A_p is the area under the plot of load versus plastic component of clip gauge opening displacement v_p corresponding to the onset of unstable brittle crack extension.The constants m and η are calculated for CT specimen using

following equations:

$$m = 3.62 - 4.21 \left(\frac{\sigma_{YS}}{\sigma_{UTS}} \right) + 4.33 \left(\frac{\sigma_{YS}}{\sigma_{UTS}} \right)^2 - 2 \left(\frac{\sigma_{YS}}{\sigma_{UTS}} \right)^3, \qquad (3.16)$$

$$\eta = -7.999 + 49.737 \left(\frac{a}{W} \right) - 78.988 \left(\frac{a}{W} \right)^2 + 41.226 \left(\frac{a}{W} \right)^3. \qquad (3.17)$$

CT specimens that were used for CTOD testing of NiTi were cut by means of electro discharge machining (EDM) from 1 mm thick sheet such that the loading direction was parallel to rolling direction (RD). The nominal dimensions and optical image of CT specimen are shown in Figure 3.18. It is worth noting that the slight difference in specimen configuration compared to the one used in K_C test allow for measurement of the load line displacement (LLD).
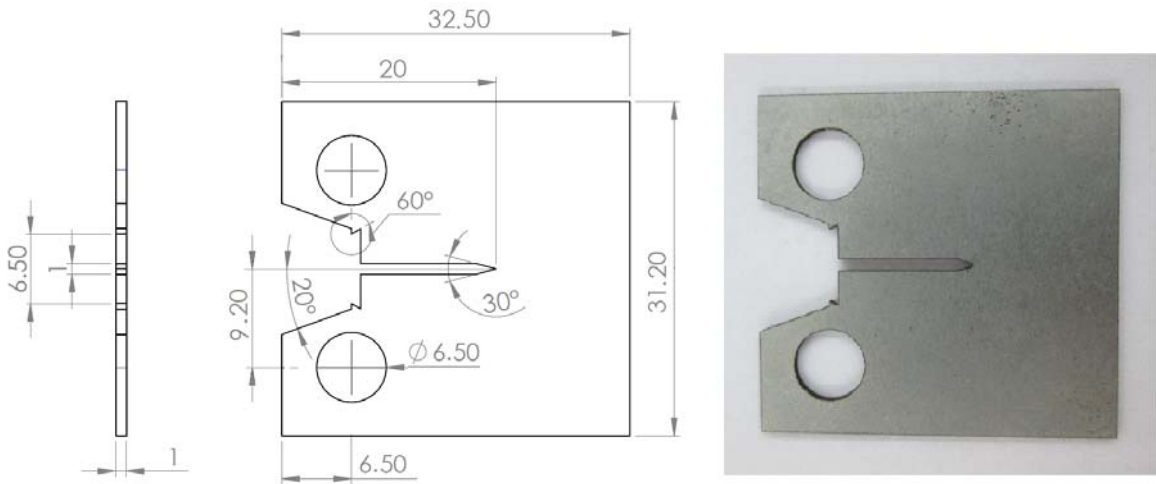
Figure 3.18. Nominal dimensions of NiTi compact tension (CT) specimen used in CTOD testing. Dimensions in mm.

To produce an ideally sharp crack, CT specimens were also fatigue pre-cracked using cyclic loading at room temperature using the servo-hydraulic INSTRON-8801 test rig with a 100 KN load cell. The experimental setup for fatigue pre-cracking was

the same as shown in Figure 3.5. Pre-cracking was performed with a frequency of 5 Hz in load control mode with sinusoidal wave form in the range 0 - 200 N using INSTRON-SAX software. Table 3.5 shows the details of fatigue pre-cracking of NiTi CT specimens for CTOD testing. It should be noted that the obtained crack sizes were within the range of ASTM E1290 ($0.45W < a < 0.7W$).

Table 3.5. Details of fatigue pre-cracking of NiTi CT specimens for CTOD testing.

	Load (N)	Cycle	Frequency (Hz)	Pre-crack Size (mm)
Specimen 1	200	7000	5	2.5
Specimen 2	200	7000	5	2.3

The optical images of pre-cracks on two specimens are illustrated in Figure 3.19. It is worth noting that the exact measurement of pre-crack sizes was carried out after final fracture using OLYMPUS 100AL optical microscopy.
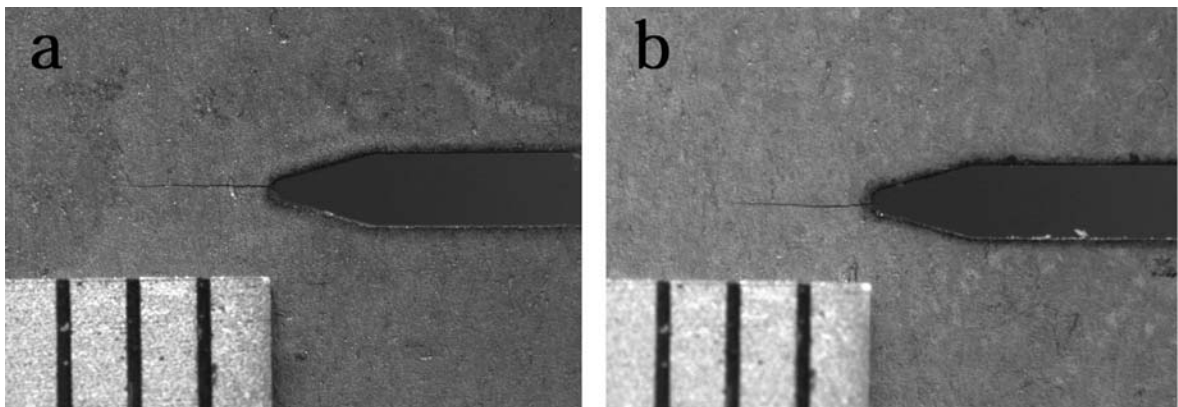
Figure 3.19. Optical images of pre-cracks on NiTi CT specimens for CTOD tests, (a) specimen 1 and (b) specimen 2.

Fracture tests were carried out using the screw-driven INSTRON-5848 test rig with a 2 KN load cell. A COD gauge was used to measure the displacement at the

load line. The experimental setup was the same as shown in Figure 3.7. An increasing displacement with a loading rate of 0.5 mm/min was applied to cracked specimens until they finally broke. Load versus clip gauge opening displacement was recorded during the test. Bluehill software was used to control the test procedure and to record the data. Similar to K_C measurements, tests were carried out at both room temperature and high temperature (100 °C) to investigate the effect of stress induced martensite transformation at the crack tip. For increasing and measuring the specimen temperature, the method explained in Section 3.1.2 was used.

3.2.3. Results and Discussion

The Load-LLD curves obtained from fracture tests on NiTi CT specimens at room temperature and high temperature are illustrated in Figures 3.20 and 3.21 respectively.
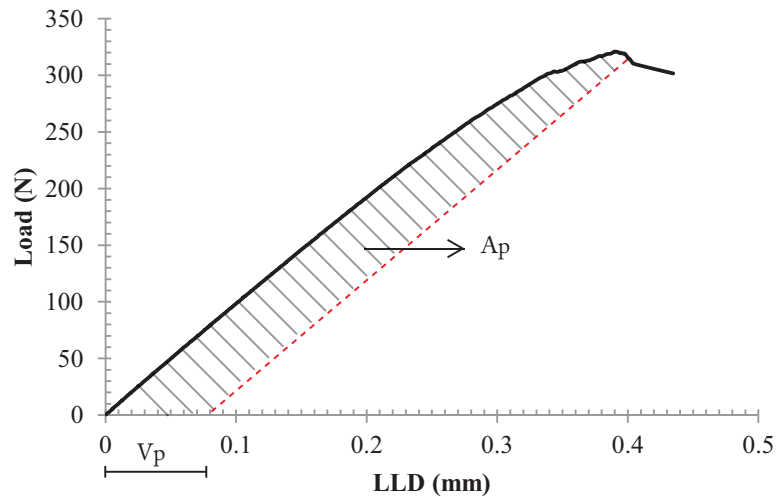
Figure 3.20. Load-LLD curve for the NiTi CT specimen with a=16 mm at room temperature.

From load-LLD curves, it could be seen that the total LLD in the curve of high temperature test is smaller compared to that of room temperature test. CTOD value at the onset of unstable brittle crack extension was obtained using Equation 3.15
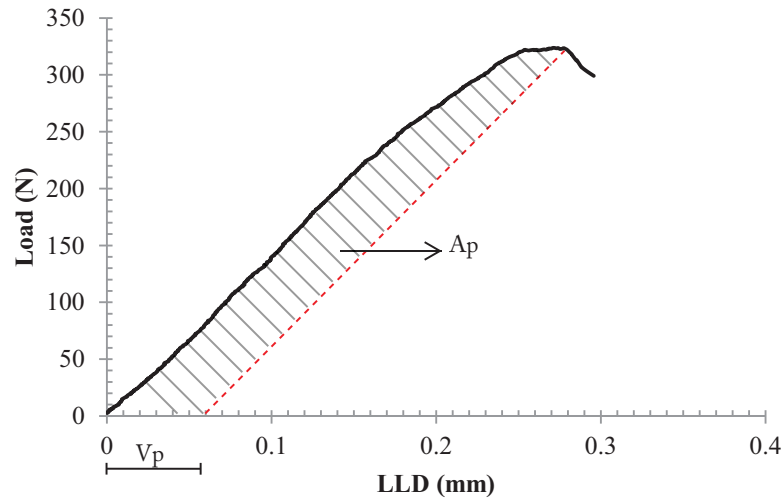
Figure 3.21. Load-LLD curve for the NiTi CT specimen with a=15.8 mm at high temperature.

where K was calculated using Equation 3.4, in which the load P obtained as the load corresponding to the onset of unstable brittle crack extension. The constants m and η were calculated using Equations 3.16 and 3.17 respectively. A_p, was obtained by constructing a line parallel to the elastic loading line in load-displacement curve. The results are illustrated in Table 3.6. Note that LLD* is the value of load line displacement corresponding to the onset of unstable brittle crack extension.

Table 3.6. Results of fracture toughness CTOD testing of NiTi CT specimens.

	a (mm)	LLD* (mm)	v_p (mm)	CTOD (mm)
Room Temperature	16	0.4	0.08	0.010
High Temperature	15.8	0.28	0.06	0.006

Comparing the results clearly illustrates that increasing the temperature above the martensite desist temperature M_d, decreases the CTOD at the onset of unstable

brittle crack extension. In other words, when the stress induced martensite transformation is suppressed at the crack tip, the specimen shows lower resistance to crack growth. This is in agreement with previous K_C measurement results indicating the toughening effect of martensite transformation in fracture of NiTi SMAs.

4. NUMERICAL INVESTIGATION OF FRACTURE BEHAVIOR

Finite elements (ABAQUS) was used to model superelastic and austenitic NiTi edge cracked specimens to compare the experimental results to numerical ones. The term superelastic NiTi is used to denote NiTi that transforms to martensite under stress, while the term austenitic NiTi is used to denote the one that does not transform. Stress distribution, phase transformation regions and displacement of crack surfaces were obtained. Fracture parameters such as stress intensity factor K_C and crack tip opening displacement CTOD were calculated using J-integral to better understand the effect of stress induced martensite transformation at the crack tip.

The ABAQUS UMAT subroutine for superelastic SMAs [53], based on Auricchio-Taylor-Lubliner constitutive model [54,55], was used to model NiTi and to input material properties. The stress-strain curve used by ABAQUS for SMA and the material properties required are shown in Figure 4.1. The material parameters used in this model were estimated from the stress-strain curves obtained from uniaxial tensile tests on NiTi specimens. In Table 4.1, the definition of parameters and their corresponding values are tabulated. Unloading and the corresponding reverse transformation are not considered because in fracture tests the specimen is directly pulled to failure. The value $\left(\frac{\delta\sigma}{\delta T}\right)_U$ was adopted from the study by Baxevanis and Lagoudas [17] because the stress-temperature curve was not determined in this study. Because at temperatures above M_d NiTi does not show a superelastic behavior, at high temperature tests, NiTi was simply modeled as an elastic material with elastic modulus of austenite obtained from tensile tests at high temperature.
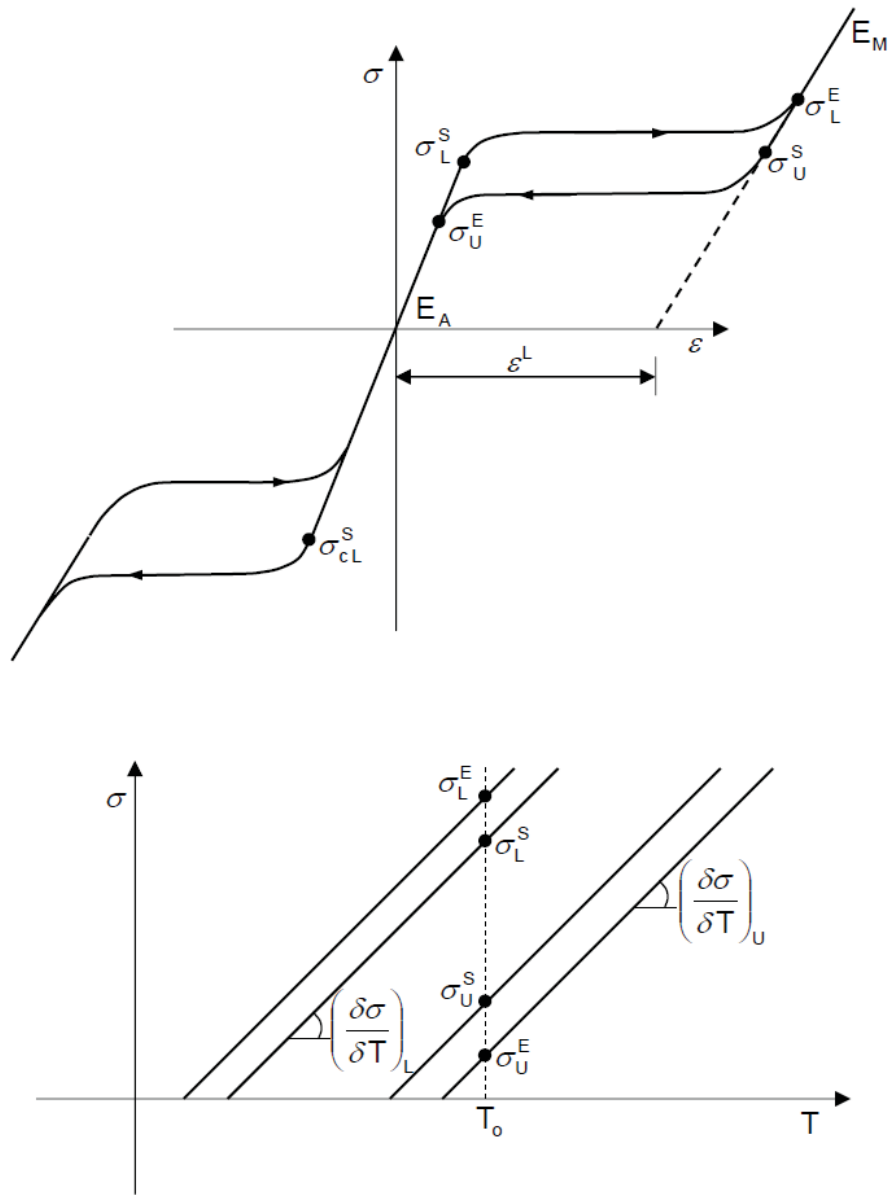
Figure 4.1. Uniaxial behavior of superelastic SMAs in UMAT subroutine.

Table 4.1. UMAT inputs used in this study.

Property	Definition	Value
E_A	Austenite elastic modulus	45 (GPa)
ν_A	Austenite Poisson's ratio	0.33
E_M	Martensite elastic modulus	14(GPa)
ν_M	Martensite Poisson's ratio	0.33
ϵ^L	Transformation strain	5 (%)
$\left(\frac{\delta\sigma}{\delta T}\right)_L$	Slope of $\sigma - T$ diagram during loading	8.7 (MPa/K)
σ_L^S	Start of forward transformation stress	400 (MPa)
σ_L^E	End of forward transformation stress	450 (MPa)
T_0	Reference temperature	300 (K)
$\left(\frac{\delta\sigma}{\delta T}\right)_U$	Slope of $\sigma - T$ diagram during unloading	8.7 (MPa/K)
σ_U^S	Start of reverse transformation stress	200 (MPa)
σ_U^E	End of reverse transformation stress	130 (MPa)
σ_{CL}^S	Start of transformation stress in compression	400 (MPa)
ϵ_V^L	Volumetric transformation strain	5 (%)
N_A	Number of annealings to be performed	0

4.1. Evaluation of Stress Intensity Factor

To model the specimen used in experiments (Figure 3.4), a 2-D plane stress finite element model was built. Due to symmetry of compact tension specimens, only the upper half of the specimen was modeled. An eight-node biquadratic plane stress quadrilateral, reduced integration element (CPS8R) was used. Mesh geometry of the 2-D specimen is illustrated in Figures 4.2. As shown in the figure, a nonuniform mesh was used by employing relatively fine mesh in the crack tip region, and coarser mesh elsewhere.

61
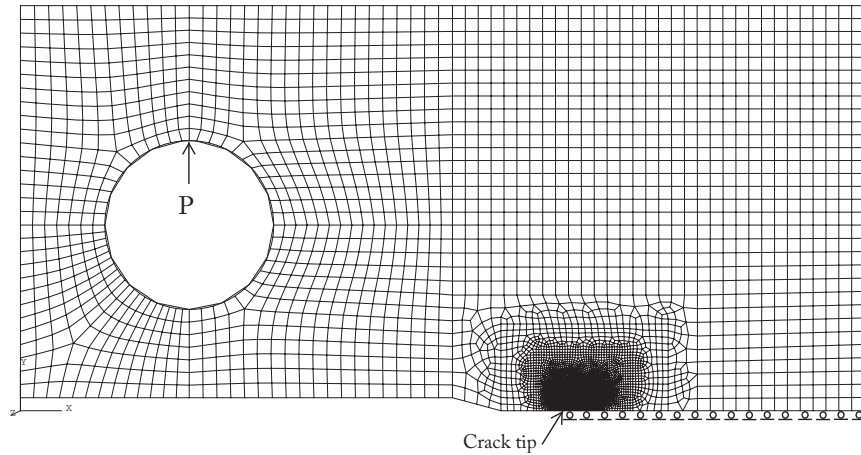
Figure 4.2. Mesh geometry of 2-D CT specimen.

A 441.4 N point load was applied i.e. the load used in K_C experiment at room temperature. Upon loading, immediately the transformation zone appeared around the crack tip. The transformation boundaries are plotted in Figure 4.3. SDV21 represents the fraction of martensite. The red shows fully transformed martensite region. The region with a dark blue color is the untransformed region. The region between these two is actually a mixture of austenite and martensite in which the fraction of martensite varies between zero and 1. The size of fully transformed region along the crack plane was measured to be 0.22 mm and total transformation zone was 1.22 mm as shown in Figure 4.3.
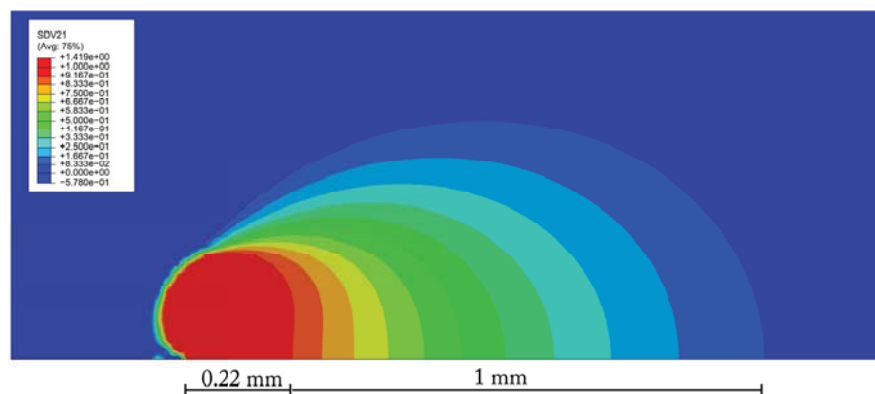
Figure 4.3. Transformation zone at the crack tip, $a = 14.3$ mm and $F = 441.4$ N.

The stress induced martensite transformation results in a more complex stress distribution. To further observe this effect, the stress distribution near the crack tip is evaluated for both superelastic and austenitic NiTi SMA. In the case of austenitic NiTi, a point load of 395.5 N i.e. the maximum load used in K_C experiment above the M_d temperature. A path was defined along the crack plane, and the stress component in loading direction (σ_{yy}) was measured along this path. The σ_{yy} distribution for superelastic and austenitic NiTi SMA are plotted in Figure 4.4.
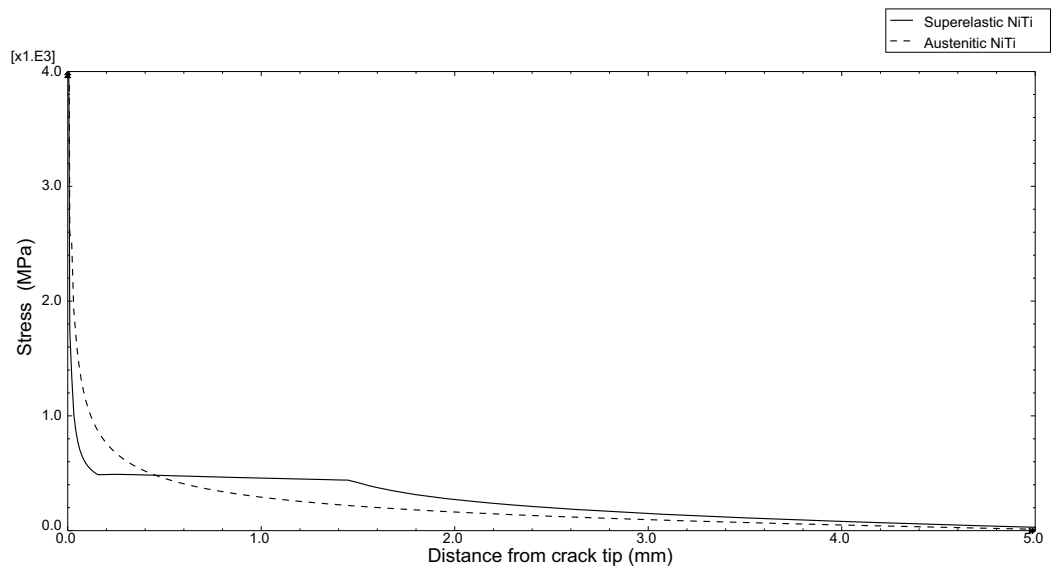
Figure 4.4. Stress distribution near the crack tip for superelastic and austenitic NiTi CT specimens.

It can be seen that in superelastic SMA the stress increases as we get closer to the crack. A stress plateau then appears as a result of stress induced transformation. Following this plateau, the stress values tend to infinity in the fully transformed martensite region at the crack tip. In austenitic model, however, the mentioned plateau is not observed and the stresses increase by getting near the crack and finally tend to infinity at the crack tip.

Because when a UMAT subroutine is used, ABAQUS does not calculate stress intensity factors directly, J-integral values are calculated first and then related to K_C

and CTOD using LEFM relations assuming a small scale transformation near the crack tip. Figure 4.5 shows the J-integral values calculated for several contours to examine the contour dependency of the values.
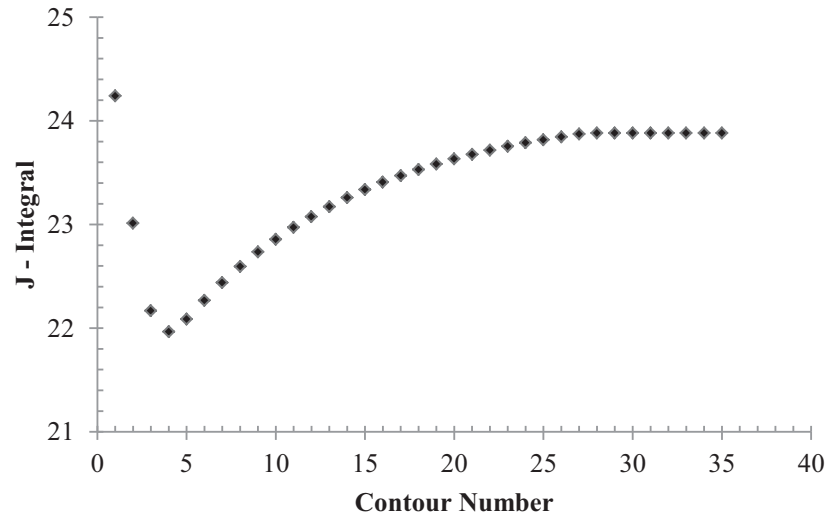
Figure 4.5. J-integral values of superelastic NiTi CT specimen, $a = 14.3$ mm and $F = 441.4$ N.

As it can be seen in this figure, the J-integral values in front of the crack tip, decrease with increasing contour number because of the non-homogenous nature of the material as a result of the stress induced martensite transformation. However, after a few contours, the values start to increase and then converge to the constant value of 23.88 KJ/m^2 indicating the fact that the J-integral values are contour independent in untransformed homogeneous region. This was later confirmed by calculating the J values for austenitic NiTi where the constant value obtained for all contours including the ones at the vicinity of crack tip.

Considering the fact that $J = G$ for linear elastic homogeneous materials and assuming that this relation can be used for the SMA as well, the stress intensity factor was calculated for both superelastic and austenitic NiTi using the equation $J = K^2/E_A$, where the J value is calculated from numerical analysis and E_A is the elastic modulus

of austenite from uniaxial tensile tests. The results are tabulated in Table 4.2.

Table 4.2. Numerical results of K_C for superelastic and austenitic NiTi SMA.

	J-integral (KJ/m^2)	K_C (MPa$\sqrt{\text{m}}$)
Superelastic NiTi	23.88	32.78
Austenitic NiTi	11.04	27.79

It can be seen that the toughness of the superelastic NiTi is larger compared to that of the austenitic NiTi, in which martensitic transformation is suppressed. This confirms the claim that transformation at the crack tip of NiTi SMA enhances the toughness of the alloy.

4.2. Crack Tip Opening Displacement

The 2-D plane stress model of the CTOD test specimen is shown in Figure 4.6. Only the upper half of the specimen was modeled due to symmetry. Like the previous model, an eight-node biquadratic plane stress quadrilateral, reduced integration element (CPS8R) was used. As shown in the figure, a nonuniform mesh was used by employing relatively fine mesh in the crack tip region, and coarser mesh elsewhere.
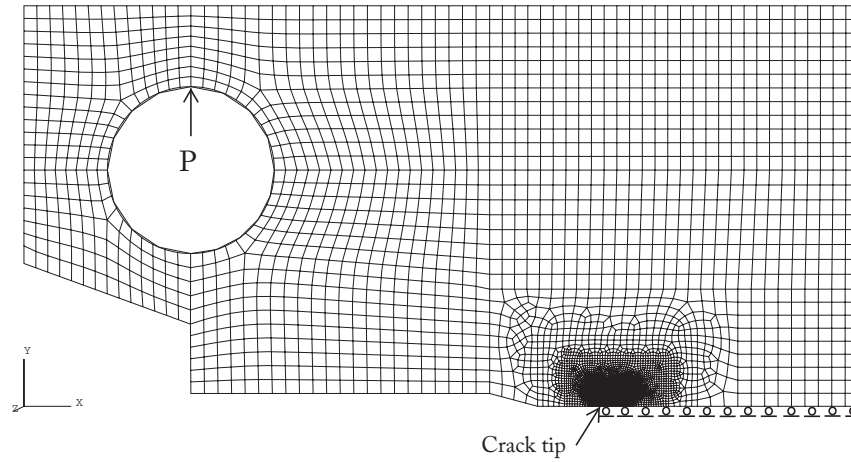
Figure 4.6. Mesh geometry of 2-D CT specimen.

A point load of 315.3 N was applied for the superelastic NiTi and a point load of 320.4 N was applied for austenitic case. These loads were the loads after which the unstable brittle crack extension was observed in experimental CTOD toughness measurements. Consequently upon applying this critical load, the CTOD value that is obtained from numerical calculations would represent the CTOD fracture toughness of NiTi SMA.

Like the previous case, a transformation zone appeared at the crack tip upon loading as shown in Figure 4.7. The size of fully transformed region along the crack plane was measured as 0.19 mm and total transformation zone was measured as 1.02 mm.
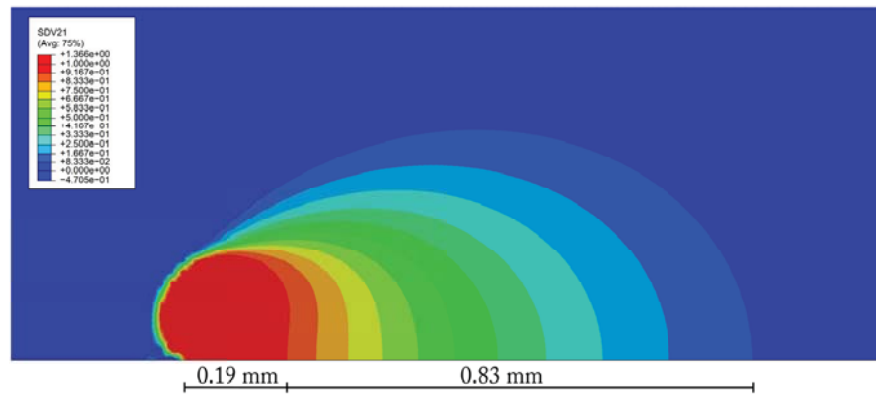
Figure 4.7. Transformation zone at the crack tip, $a = 16$ mm and $F = 315.3$ N.

The displacement (u_y) along the crack surfaces for superelastic and austenitic models is plotted in Figure 4.8. The displacements were measured under the applied load at which unstable brittle crack growth occured. From the plot, it can be seen that all displacement values along the crack surface for the superelastic NiTi are larger than that of austenitic one. Consequently, it can be predicted that the displacement at the crack tip (CTOD) would be larger as well.
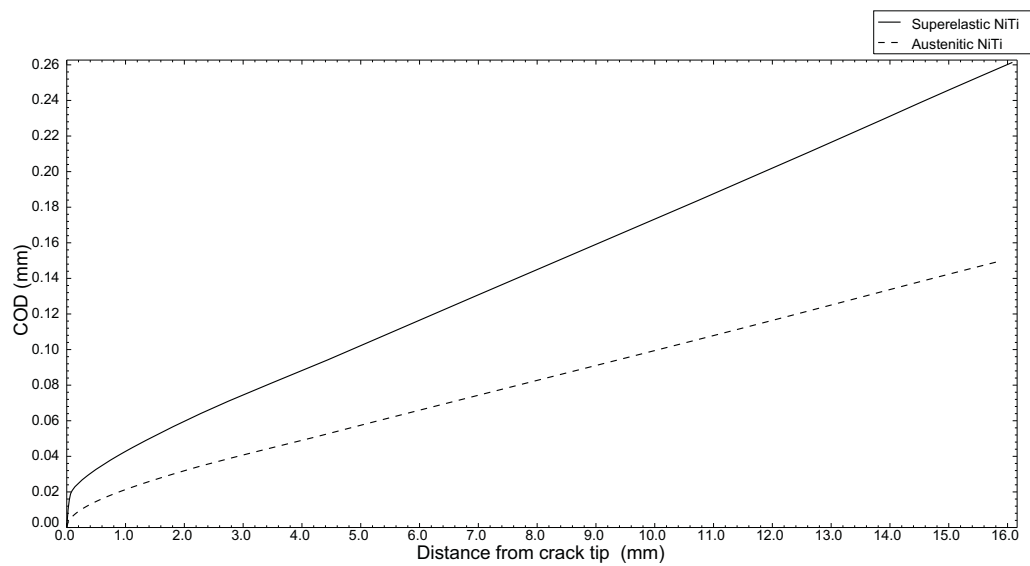
Figure 4.8. Displacement along the crack surface for superelastic and austenitic NiTi CT specimens.

J-integral values calculated for several contours as shown in Figure 4.9. In supere-
lastic NiTi, the J values converge to the constant value of 19.88 KJ/m^2 after certain
number of contours. On the other hand, for austenitic NiTi, the constant value of 11.14
KJ/m^2 was obtained for all contours including the ones at the vicinity of crack tip.
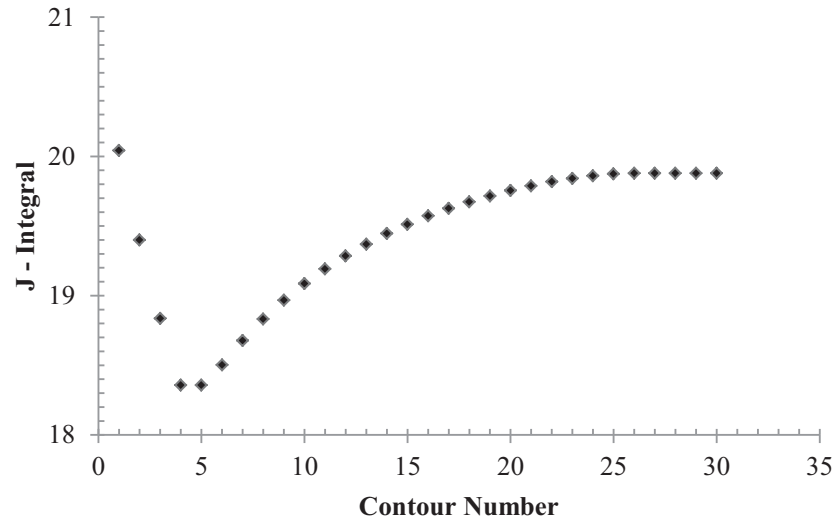
Figure 4.9. J-integral values of superelastic NiTi CT specimen, $a = 16$ mm and
$F = 315.3$ N.

CTOD toughness values are then obtained for both superelastic and austenitic
NiTi using Equation 3.14 and assuming that $d_n = 1$ as shown in Table 4.3.

Table 4.3. Numerical results of fracture toughness CTOD of superelastic and
austenitic NiTi.

	J-integral (KJ/m^2)	CTOD (mm)
Superelastic NiTi	19.88	0.011
Austenitic NiTi	11.14	0.008

According to the results, it could be seen that the superelastic NiTi has a higher CTOD value as expected, indicating the toughening effect of stress induced martensite transformation at the crack tip of NiTi SMAs. This is in agreement with previous results of K_C analyzes.

4.3. Comparison of Experimental and Numerical Results

K_C and CTOD values obtained from experimental measurements and numerical calculations are tabulated in Table 4.4. Experimental results indicate that both K_C and CTOD values decrease when stress induced martensite transformation at the crack tip is blocked the difference being more considerable for CTOD. The same trend is observed in numerical results. In finite element results, both K_C and CTOD are larger for the superelastic NiTi. Similar to the experiments, the difference between CTOD values are much more than K_C. The experimental and numerical results are in good agreement, indicating the toughening effect of phase transformation in fracture behavior of NiTi SMAs.

Table 4.4. Comparison of experimental and numerical results.

	Material State	K_C (MPa$\sqrt{m}$)	CTOD (mm)
Experimental	Superelastic	31.9	0.010
	Austenitic	28.1	0.006
Numerical	Superelastic	32.78	0.011
	Austenitic	27.79	0.008

5. SUMMARY AND CONCLUSIONS

In this study the effect of stress induced martensite transformation on fracture parameters of NiTi SMA was investigated numerically and experimentally. The microstructure of thin sheets of NiTi was examined using optical microscopy to obtain average grain size. Uniaxial tensile tests were carried out at room temperature and stress-strain curves were obtained for 1 mm thick dog-bone specimens in both rolling (RD) and transverse (TD) directions to determine the mechanical properties of the alloy. The material tensile strength, austenite and martensite elastic moduli, transformation stress and strain were measured. Tensile tests were repeated at $100\,^{\circ}$C to measure the properties in the absence of martensitic phase transformation. It should be noted that the martensite elastic modulus obtained from the stress-strain curves, does not represent the true modulus of martensite and alternative techniques such as neutron diffraction measurements should be used to measure the true elastic modulus of martensite.

Fatigue pre-cracked compact tension (CT) specimens with 1 mm thickness were used to study the fracture toughness of the NiTi SMA at both room temperature and high temperature. Load versus crack mouth opening displacement (CMOD) curves were plotted and the K_C values were calculated using LEFM principles. Considering the fact that LEFM is valid as long as nonlinear material deformation is confined to a very small region surrounding the crack tip, EPFM principles were implemented to measure an alternative fracture parameter. CTOD values were measured using load versus load line displacement (LLD) curves. The results revealed that for both parameters, the fracture toughness of the NiTi SMA decreases if temperature increases above martensite desist temperature M_d.

Superelastic and austenitic 2-D cracked CT specimens were also analyzed using finite elements. ABAQUS UMAT subroutine for superelastic alloys was implemented to define the superelastic behavior. Transformation boundaries were determined. Displacement and stress distribution near the crack tip were calculated. J-integral values

were calculated and used to obtain K_C and CTOD values. It was observed that the J-integral values are contour dependant near the crack tip of superelastic NiTi because of the non-homogenous nature of the material as a result of the stress induced martensite transformation. Consequently, the J values obtained from untransformed homogeneous region were used to calculate K_C and CTOD. The results showed that the fracture toughness of the superelastic NiTi is higher as a result of martensitic transformation.

A good agreement was observed between numerical and experimental results in terms of K_C and CTOD. In addition, in both analyses, a decrease in fracture toughness was observed when the stress induced martensite transformation was suppressed, indicating that transformation ahead of the crack tip improves the toughness of NiTi SMA. This conclusion is in agreement with most of the previous studies on fracture of SMAs [2, 8, 14, 21, 26, 29], in which the toughening effect of the martensitic transformation has been reported. However, it is in contrast with few studies [18, 36]. Consequently, the effect of martensitic transformation at the crack tip of NiTi SMAs still needs further investigation.

REFERENCES

1. Lagoudas, D., *Shape Memory Alloys: Modeling and Engineering Applications*, Springer, 2010.

2. Daly, S., A. Miller, G. Ravichandran and K. Bhattacharya, "An Experimental Investigation of Crack Initiation in Thin Sheets of Nitinol", *Acta Materialia*, Vol. 55, No. 18, pp. 6322–6330, 2007.

3. Jannetti, C. V., *Martensitic Phase Transformation in Shape Memory Alloys: Constitutive Modeling and Numerical Simulation*, Ph.D. Thesis, University of Pennsylvania, 2005.

4. Liang, C., *The Constitutive Modeling of Shape Memory Alloys*, Ph.D. Thesis, Virginia Polytechnic Institute and State University, 1990.

5. Saadat, S., J. Salichs, M. Noori, Z. Hou, H. Davoodi, I. Bar-On, Y. Suzuki and A. Masuda, "An Overview of Vibration and Seismic Applications of NiTi Shape Memory Alloy", *Smart Materials and Structures*, Vol. 11, No. 2, p. 218, 2002.

6. Stam, G. and E. van der Giessen, "Effect of Reversible Phase Transformations on Crack Growth", *Mechanics of Materials*, Vol. 21, No. 1, pp. 51 – 71, 1995.

7. Birman, V., "On Mode I Fracture of Shape Memory Alloy Plates", *Smart Materials and Structures*, Vol. 7, pp. 433–437, 1998.

8. Yi, S. and S. Gao, "Fracture Toughening Mechanism of Shape Memory Alloys due to Martensite Transformation", *International Journal of Solids and Structures*, Vol. 37, No. 38, pp. 5315–5327, 2000.

9. Yi, S., S. Gao and L. Shen, "Fracture Toughening Mechanism of Shape Memory Alloys under Mixed-Mode Loading due to Martensite Transformation", *International*

Journal of Solids and Structures, Vol. 38, No. 24–25, pp. 4463 – 4476, 2001.

10. Yan, W., C. H. Wang, X. P. Zhang and Y.-W. Mai, "Theoretical Modelling of the Effect of Plasticity on Reverse Transformation in Superelastic Shape Memory Alloys", *Materials Science and Engineering: A*, Vol. 354, No. 1, pp. 146–157, 2003.

11. Lexcellent, C. and F. Thiebaud, "Determination of the Phase Transformation Zone at a Crack Tip in a Shape Memory Alloy Exhibiting Asymmetry between Tension and Compression", *Scripta Materialia*, Vol. 59, No. 3, pp. 321 – 323, 2008.

12. Maletta, C. and F. Furgiuele, "Analytical Modeling of Stress-Induced Martensitic Transformation in the Crack Tip Region of Nickel–Titanium Alloys", *Acta Materialia*, Vol. 58, No. 1, pp. 92–101, 2010.

13. Lexcellent, C., M. Laydi and V. Taillebot, "Analytical Prediction of the Phase Transformation Onset Zone at a Crack Tip of a Shape Memory Alloy Exhibiting Asymmetry Between Tension and Compression", *International Journal of Fracture*, Vol. 169, No. 1, pp. 1–13, 2011.

14. Maletta, C. and F. Furgiuele, "Fracture Control Parameters for NiTi Based Shape Memory Alloys", *International Journal of Solids and Structures*, Vol. 48, No. 11–12, pp. 1658–1664, 2011.

15. Maletta, C. and M. Young, "Stress-Induced Martensite in Front of Crack Tips in NiTi Shape Memory Alloys: Modeling Versus Experiments", *Journal of Materials Engineering and Performance*, Vol. 20, No. 4-5, pp. 597–604, 2011.

16. Maletta, C., "A Novel Fracture Mechanics Approach for Shape Memory Alloys with Trilinear Stress–Strain Behavior", *International Journal of Fracture*, Vol. 177, No. 1, pp. 39–51, 2012.

17. Baxevanis, T. and D. Lagoudas, "A Mode I Fracture Analysis of a Center-Cracked Infinite Shape Memory Alloy Plate under Plane Stress", *International Journal of*

Fracture, Vol. 175, No. 2, pp. 151–166, 2012.

18. Yan, W., C. Wang, X. Zhang and Y. Mai, "Effect of Transformation Volume Contraction on the Toughness of Superelastic Shape Memory Alloys", *Smart Materials and Structures*, Vol. 11, pp. 947–955, 2002.

19. Wang, X., Y. Wang, A. Baruj, G. Eggeler and Z. Yue, "On the Formation of Martensite in front of Cracks in Pseudoelastic Shape Memory Alloys", *Materials Science and Engineering: A*, Vol. 394, No. 1–2, pp. 393–398, 2005.

20. Wang, G., "Effects of Notch Geometry on Stress–Strain Distribution, Martensite Transformation and Fracture Behavior in Shape Memory Alloy NiTi", *Materials Science and Engineering: A*, Vol. 434, No. 1–2, pp. 269–279, 2006.

21. Wang, G., "Effect of Martensite Transformation on Fracture Behavior of Shape Memory Alloy NiTi in a Notched Specimen", *International Journal of Fracture*, Vol. 146, No. 1-2, pp. 93–104, 2007.

22. Freed, Y. and L. Banks-Sills, "Crack Growth Resistance of Shape Memory Alloys by means of a Cohesive Zone Model", *Journal of the Mechanics and Physics of Solids*, Vol. 55, No. 10, pp. 2157–2180, 2007.

23. Wang, G., "A Finite Element Analysis of Evolution of Stress–Strain and Martensite Transformation in front of a Notch in Shape Memory Alloy NiTi", *Materials Science and Engineering: A*, Vol. 460–461, No. 0, pp. 383–391, 2007.

24. Falvo, A., F. Furgiuele, A. Leonardi and C. Maletta, "Stress-Induced Martensitic Transformation in the Crack Tip Region of a NiTi Alloy", *Journal of Materials Engineering and Performance*, Vol. 18, No. 5-6, pp. 679–685, 2009.

25. Baxevanis, T., Y. Chemisky and D. Lagoudas, "Finite Element Analysis of the Plane Strain Crack-Tip Mechanical Fields in Pseudoelastic Shape Memory Alloys", *Smart Materials and Structures*, Vol. 21, 2012.

26. Baxevanis, T., A. Parrinello and D. Lagoudas, "On the Fracture Toughness Enhancement due to Stress-Induced Phase Transformation in Shape Memory Alloys", *International Journal of Plasticity*, 2013.

27. Gall, K., N. Yang, H. Sehitoglu and Y. Chumlyakov, "Fracture of Precipitated NiTi Shape Memory Alloys", *International Journal of Fracture*, Vol. 109, No. 2, pp. 189–207, 2001.

28. Tong, W., H. Tao and N. Zhang, "Crack Initiation and Growth in a Notched NiTi Shape Memory Alloy Sheet", *MRS Proceedings*, Vol. 785, 2003.

29. Chen, J., G. Wang and W. Sun, "Investigation on the Fracture Behavior of Shape Memory Alloy NiTi", *Metallurgical and Materials Transactions A*, Vol. 36, No. 4, pp. 941–955, 2005.

30. Robertson, S., A. Mehta, A. Pelton and R. Ritchie, "Evolution of Crack-Tip Transformation Zones in Superelastic Nitinol Subjected to in-Situ Fatigue: A Fracture Mechanics and Synchrotron X-Ray Microdiffraction Analysis", *Acta Materialia*, Vol. 55, No. 18, pp. 6198–6207, 2007.

31. Jiang, F. and K. S. Vecchio, "Fracture of Nitinol under Quasistatic and Dynamic Loading", *Metallurgical and Materials Transactions A*, Vol. 38, No. 12, pp. 2907–2915, 2007.

32. Wang, X., B. Xu, Z. Yue and X. Tong, "Fracture Behavior of the Compact Tension Specimens in NiTi Shape Memory Alloys", *Materials Science and Engineering: A*, Vol. 485, No. 1–2, pp. 14–19, 2008.

33. Gollerthan, S., D. Herberg, A. Baruj and G. Eggeler, "Compact Tension Testing of Martensitic/Pseudoplastic NiTi Shape Memory Alloys", *Materials Science and Engineering: A*, Vol. 481–482, pp. 156 – 159, 2008.

34. Creuziger, A., L. Bartol, K. Gall and W. Crone, "Fracture in Single Crystal NiTi",

Journal of the Mechanics and Physics of Solids, Vol. 56, No. 9, pp. 2896–2905, 2008.

35. Wang, X., Z. Lu and Z. Yue, "The Effect of Notches on the Fracture Behavior in NiTi Shape Memory Alloys", *International Journal of Solids and Structures*, Vol. 46, No. 3–4, pp. 557–571, 2009.

36. Gollerthan, S., M. Young, A. Baruj, J. Frenzel, W. Schmahl and G. Eggeler, "Fracture Mechanics and Microstructure in NiTi Shape Memory Alloys", *Acta Materialia*, Vol. 57, No. 4, pp. 1015–1025, 2009.

37. Jiang, S., Y. Zhang and H. Fan, "Fracture Behavior and Microstructure of as-cast NiTi Shape Memory Alloy", *Transactions of Nonferrous Metals Society of China*, Vol. 22, No. 6, pp. 1401–1406, 2012.

38. Maletta, C., E. Sgambitterra and F. Furgiuele, "Crack Tip Stress Distribution and Stress Intensity Factor in Shape Memory Alloys", *Fatigue and Fracture of Engineering Materials and Structures*, 2013.

39. ASTM, "Designation F2063-12 : Standard Specification for Wrought Nickel-Titanium Shape Memory Alloys for Medical Devices and Surgical Implants", *Annual Book of ASTM Standards*, Vol. 13.01, 2013.

40. ASTM, "Designation E8/E8m-11 : Standard Test Methods for Tension Testing of Metallic Materials", *Annual Book of ASTM Standards*, Vol. 13.01, 2012.

41. ASTM, "Designation F2516-07 : Standard Test Method for Tension Testing of Nickel-Titanium Superelastic Materials", *Annual Book of ASTM Standards*, Vol. 13.02, 2008.

42. Wagner, M. and W. Windl, "Lattice Stability, Elastic Constants and Macroscopic Moduli of NiTi Martensites from First Principles", *Acta Materialia*, Vol. 56, pp. 6232–6245, 2008.

43. Liu, Y. and H. Xiang, "Apparent Modulus of Elasticity of Near-Equiatomic NiTi", *Journal of Alloys and Compounds*, Vol. 270, pp. 154–159, 1998.

44. Anderson, T., *Fracture Mechanics: Fundamentals and Applications*, Taylor and Francis, 2005.

45. Dowling, N., *Mechanical Behavior of Materials: Engineering Methods for Deformation, Fracture, and Fatigue*, Pearson Prentice Hall, 2007.

46. ASTM, "Designation E399-12 : Standard Test Method for Linear-Elastic Plane-Strain Fracture Toughness K_{IC} of Metallic Materials", *Annual Book of ASTM Standards*, Vol. 03.01, 2013.

47. ASTM, "Designation E1921-13 : Standard Test Method for Determination of Reference Temperature, T_0, for Ferritic Steels in the Transition Range1", *Annual Book of ASTM Standards*, Vol. 03.01, 2013.

48. Wells, A., "Unstable Crack Propagation in Meials: Cleavage and Fast Fracture", *Crack Propagation Symposium*, 1961.

49. Burdekin, F. M. and D. Stone, "The Crack Opening Displacement Approach to Fracture Mechanics in Yielding Materials", *The Journal of Strain Analysis for Engineering Design*, Vol. 1, No. 2, pp. 145–153, 1966.

50. Rice, J. R., "A Path Independent Integral and Approximate Analysis of Strain Concentration by Notches and Cracks", *Journal of Applied Mechanics*, Vol. 35, pp. 379–386, 1968.

51. Shih, C. F., "Relationships Between the J-Integral and the Crack Opening Displacement for Stationary and Extending Cracks", *Journal of the Mechanics and Physics of Solids*, Vol. 29, pp. 305–326, 1980.

52. ASTM, "Designation E1290-08 : Standard Test Method for Crack-Tip Opening

Displacement (CTOD) Fracture Toughness Measurement", *Annual Book of ASTM Standards*, Vol. 03.01, 2008.

53. ABAQUS, "UMAT and VUMAT Routines for the Simulation of Nitinol", Answer ID 1658, ABAQUS Inc., Pawtucket, RI.

54. Auricchio, F. and R. L. Taylor, "Shape-Memory Alloys: Modeling and Numerical Simulations of the Finite-Strain Superelastic Behavior", *Computer Methods in Applied Mechanics and Engineering*, Vol. 143, pp. 175–194, 1997.

55. Auricchio, F., R. L. Taylor and J. Lubliner, "Shape-Memory Alloys: Macromodeling and Numerical Simulations of the Superelastic Behavior", *Computer Methods in Applied Mechanics and Engineering*, Vol. 146, pp. 281–312, 1997.